International Journal for Numerical and Analytical Methods in Geomechanics

WILEY

RESEARCH ARTICLE

Suspended Sediment Transport in Ice-Covered Turbulent Flow: Semi-Analytical Solution and Parametric Sensitivity

Sourav Hossain[1] | Ashok Das[2] | Sanjib Naskar[3] | Sweta Narayan Sahu[4] | Koeli Ghoshal[4]

[1]Department of Civil Engineering, National Taiwan University, Taipei, Taiwan | [2]Department of Mathematics and Computing, IIT(ISM) Dhanbad, Dhanbad, Jharkhand, India | [3]Department of Mathematics, Siksha 'O' Anusandhan Deemed to be University, Bhubaneswar, Odisha, India | [4]Department of Mathematics, IIT Kharagpur, Kharagpur, West Bengal, India

Correspondence: Ashok Das (ashokdas@iitism.ac.in)

Received: 3 August 2025 | **Revised:** 18 November 2025 | **Accepted:** 26 November 2025

Keywords: ice-covered channel flow | integral transform | semi-analytical solution | suspended sediment transport

ABSTRACT

This study presents a semi-analytical solution for modeling suspended sediment distribution in turbulent flows within ice-covered channels under unsteady, non-equilibrium conditions. The solution is derived using the generalized integral transform technique (GITT). Validation was performed against the cell-centered finite volume method and existing experimental data. The results confirm high accuracy, supported by error analysis. Optimized parameter values were obtained through a hybrid genetic and interior point algorithm. Several underlying phenomena of particle-turbulence interactions in ice-covered channels are explored. The focus is on the influence of key sediment transport parameters on the time-dependent evolution of vertical concentration profiles of suspended sediment particles. Key findings indicate that increasing the settling-velocity correction coefficient raises sediment concentration profiles over time. In contrast, greater ice-cover roughness reduces sediment suspension. Sensitivity analysis highlights the inverse of the Schmidt number as a critical factor. This novel application of GITT and variance-based sensitivity analysis (VBSA) provides a detailed solution library, and serves as a benchmark for numerical models.

1 | Introduction

In regions with freezing temperatures, ice-covered channels can be natural or artificial. These channels have unique geometries and hydraulic behaviors compared to open channels. Such characteristics significantly influence sediment transport [1–5]. The role of ice cover in sediment dynamics is not well understood. This knowledge gap limits its application in hydraulic infrastructure design [1] and increases the risk of structural damage in freezing environments [6]. A detailed understanding of sediment transport in ice-covered channels is essential. It is key to improving management strategies and making accurate predictions.

Flow in an ice-covered channel is fully developed, asymmetric, and turbulent. This is due to differing hydraulic roughness at the top and bottom boundaries [7]. Turbulence from both boundaries mixes across the flow depth. This mixing is most noticeable within the central core. It affects sediment transport [7]. Ice cover increases resistance and reduces bulk flow velocity. It amplifies total boundary shear stress and redistributes it between the boundaries. This redistribution impacts bed load transport by altering drag on the channel bed [8]. It also affects suspended load transport by modifying turbulent diffusivity [9].

Suspended sediment transport is different from bed-load transport, as it is vertically dispersed by turbulence. It plays a critical role in shaping water bodies, geological formations, and engineering applications. Accurate prediction of suspended sediment dynamics is essential. Extensive research has investigated suspended sediment in open-channel flows [10–19], including

experimental, analytical, semi-analytical, and numerical studies. In a recent study, Zhang et al. [20] derived an analytical solution for the vertical distribution of suspended sediment concentration under unsteady conditions and proposed an optimization framework for simultaneously estimating the governing physical parameters. Recent studies have also highlighted the growing role of statistical learning approaches in suspended sediment transport. Temporal LASSO regression has been employed by Zhang et al. [21] for suspended sediment concentration forecasting, providing high accuracy and interpretable variable selection. Augmented lncosh ridge regression with empirical mode decomposition was applied by Zhang et al. [22] for suspended sediment concentration predictions using suspended sediment concentration-only data, effectively handling outliers and temporal correlations. Decomposition-based regression frameworks have been used by Zhang et al. [23] to infer sediment transport parameters from field suspended sediment concentration time series, incorporating stormwave and tidal effects. However, studies on ice-covered channels, whether experimental, analytical, semi-analytical, or numerical, remain limited. This limitation is due to their complex flow characteristics.

Sayre and Song [8] conducted flume experiments to study the impact of ice cover. They divided the flow into upper ice and lower bed layers. Maximum streamwise velocity and zero turbulent shear stress were observed at their junction. Krishnappan [24] used the $k - \epsilon$ model to derive momentum diffusivity and develop sediment concentration profiles. Their results showed lower relative sediment concentration in ice-covered flows compared to open flows under similar conditions. Further reductions were observed as the ice-to-bed roughness ratio increased. Lau and Krishnappan [25] extended this approach to analyze sediment concentration and velocity distribution in ice-covered channels. Numerical models by Knack [26] and Huang [27] incorporated hydro-thermo-ice-sediment dynamics. These models were used to study sediment transport in curved channels. Knack and Shen [28] modified the Rouse formula. They integrated the effects of ice cover on velocity and diffusion to estimate sediment transport rates. Wang et al. [29] developed a steady one-dimensional (1D) model for sediment concentration in ice-covered alluvial channels. This model solved the Schmidt–O'Brian equation with established settling velocity and diffusivity formulations. Wang et al. [1] developed a random displacement model for sediment transport in ice-covered alluvial channels. Wang et al. [30] proposed an equation to capture the nonlocal transport of sediment particles in steady, uniform, ice-covered channel flows. This equation was based on a steady fractional advection-diffusion framework. Huai et al. [31] estimated the suspended sediment concentration in ice-covered channels using gravitational theory. Sahu et al. [32] analyzed time-dependent sediment concentration under steady uniform flow in an ice-covered channel. They used a numerical finite difference scheme for their analysis. Sahu et al. [33] employed a fractional advection–diffusion equation (fADE). This was used to numerically predict suspension concentration in an ice-covered channel. Sahu and Ghoshal [34] recently employed a semi-analytical approach based on the Riccati equation to solve a steady, one-dimensional coupled model of velocity and suspension concentration in an ice-covered channel. Their formulation considers variation only in the vertical direction and neglects temporal dependence, thereby reducing the governing equations to a set of ordinary differential equations (ODEs).

The analytical model by Sayre and Song [8] is predictive but has limitations. It requires prior knowledge of the streamwise velocity profile. It also assumes a less rigorous linear trend for the turbulent diffusion coefficient. Additionally, its diffusion coefficient components are not unified into a single equation. Wang et al. [29] improved upon this model. Their approach offered better predictions of concentration distribution in suspension regions. However, both models are steady and one-dimensional, and rely on simple ODEs that are easy to solve. Numerical models by Krishnappan [24] and Lau and Krishnappan [25] are accurate but demand significant computational effort. They also lack clarity on the physical factors influencing sediment concentration. Similarly, the hydro-thermo-ice-sediment models by Khader [35] and Huang [27] are complex. These models require extensive calculations. The recent unsteady two-dimensional (2D) and 1D models by Sahu et al. [32] and Sahu et al. [33] offer valuable insights. However, they rely on numerical methods that are prone to errors. More recently, Sahu et al. [36] obtained an analytical solution of a one-dimensional time-fractional advection–diffusion equation using Laplace and Fourier transforms to investigate the time-dependent memory effects of particles in ice-covered channel flows.

To date, analytical and semi-analytical models based on classical calculus theory for suspension concentration in ice-covered channels have been mostly limited to steady, one-dimensional frameworks. This limitation is due to the complexity of solving partial differential equations (PDEs) with time-dependent components. This study addresses this gap. It applies the generalized integral transform technique (GITT) to solve an unsteady 1D suspended sediment transport problem in an ice-covered channel flow. Solving PDEs analytically is not straightforward. However, addressing an unsteady one-dimensional model analytically or semi-analytically can provide deep insights. It can also contribute to the development of new ideas. GITT [37–39] is chosen due to its flexibility in constructing integral transform pairs. These pairs include forward and inverse transforms. GITT also allows for relative ease in mathematically manipulating these resulting pairs. The use of GITT for sediment transport in turbulent flows is limited. Liu and Nayamatullah [13] derived a semi-analytical solution for unsteady 1D transport. Similarly, Liu [40] developed an analytical solution for steady 2D suspended sediment transport. Both studies focused on turbulent flow conditions. However, they were restricted to open channel configurations. Similar applications of such problems can be observed in atmospheric sciences. Studies like Wortmann et al. [41], Costa et al. [42], Moreira et al. [43], Buske et al. [44], and Cassol et al. [45] used GITT for their solution methodologies. These studies simulated pollutant dispersion in the planetary boundary layer. It is pertinent to note that although analytical and semi-analytical solutions have long been fundamental in sediment and hydraulic engineering, their applicability is often limited by simplifying assumptions required to represent complex flow environments [46]. More recently, Zhang et al. [46] explored the use of physics-informed neural networks (PINNs) for one-dimensional vertical (1DV) suspended sediment concentration, offering a framework free from the discretization errors and approximations inherent in conventional numerical methods.

The primary objectives of this study are as follows: (i) to present a semi-analytical solution for an unsteady one-dimensional model

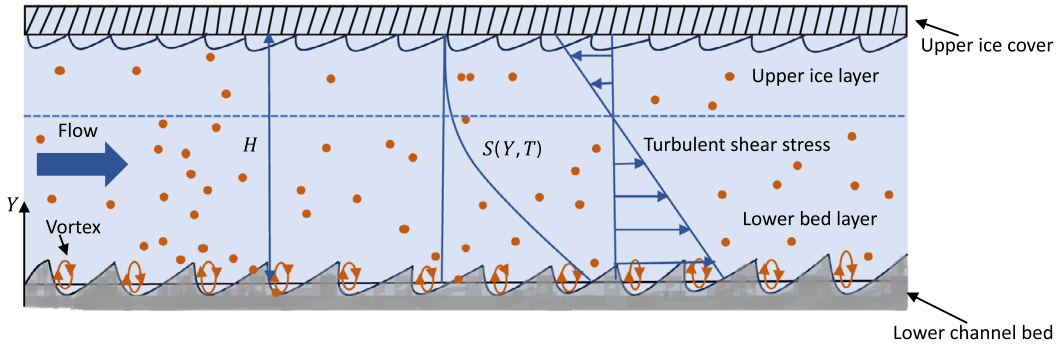

FIGURE 1 | Schematic diagram of an ice-covered channel transporting suspended sediment particles (adapted from Wang et al. [29]).

to predict the temporal evolution of suspended concentration profiles in turbulent flow within a wide ice-covered channel using GITT, (ii) to validate the proposed GITT solution by comparing it with a cell-centered finite volume method, (iii) to analyze the impact of various hydraulic parameters on concentration magnitudes, (iv) to assess the capability of the proposed model to accurately predict available experimental data, and (v) to estimate optimized values and conduct sensitivity analyses of key sediment transport parameters based on available observations, facilitating easier applicability of the model.

It is generally acknowledged that ice-covered turbulent flows are inherently complex and three-dimensional. However, the present study focuses on developing a one-dimensional unsteady vertical transport model to capture the essential features of sediment transport under an ice cover in a computationally efficient manner. The one-dimensional vertical approach allows us to isolate and analyze the dominant vertical diffusion processes influenced by the ice cover while avoiding the high computational cost and data requirements associated with fully three-dimensional modeling. This simplification is particularly suitable for examining the time-dependent variation of suspended sediment concentration. Nevertheless, we acknowledge that this assumption limits the model's ability to represent various turbulent structures that may arise in natural ice-covered channels. These effects can influence sediment dynamics, especially in non-uniform geometries or near channel boundaries. Therefore, the present model should be viewed as a foundational framework that provides physical insight into vertical transport mechanisms and can be further extended or coupled with higher-dimensional models in future studies.

2 | Problem Description

2.1 | Governing Equation

The investigation commences by considering the following unsteady 1D mathematical model depicting the transport of suspended sediment within an ice-covered channel (see Figure 1):

$$\frac{\partial S(Y,T)}{\partial T} - \frac{\partial}{\partial Y}[\omega(Y)S(Y,T)] = \frac{\partial}{\partial Y}\left[\nu(Y)\frac{\partial S(Y,T)}{\partial Y}\right]. \quad (1)$$

In Equation (1), S denotes the concentration of suspended sediment (mg/L), T represents time (s), $\omega(Y)$ denotes the downward velocity of sediment settling (m/s), and $\nu(Y)$ stands for the sediment diffusion coefficient (m^2/s). Both $\omega(Y)$ and $\nu(Y)$ are assumed to be functions solely dependent on the vertical coordinate Y (m). To derive the concentration profile from Equation (1), it is necessary to discern the spatial variations of the sediment diffusion coefficient, $\nu(Y)$, and the sediment settling velocity, $\omega(Y)$. As illustrated in Figure 1, a turbulent stream of water first enters an erodible sediment bed within an ice-covered channel. It then interacts with the sediment particles, causing them to diffuse into the main turbulent flow until equilibrium is achieved.

The sediment diffusion coefficient, $\nu(Y)$, is commonly associated with the turbulent diffusion coefficient, $\nu_t(Y)$, through a dimensionless constant referred to as the inverse of the turbulent Schmidt number, denoted by Λ. This relationship is expressed as follows [24]:

$$\nu(Y) = \Lambda\nu_t(Y). \quad (2)$$

In the study of flow within an ice-covered channel, the disparity in roughness between the channel bed and the ice cover necessitates the consideration of two distinct sets of length and velocity scales governing turbulent mixing. Guo et al. [47] amalgamated these scales into a unified equation and proposed the ensuing expression for the turbulent diffusion coefficient $\nu_t(Y)$ as

$$\nu_t(Y) = 2\kappa H U_{*B}\beta\frac{Y}{H}\left(1-\frac{Y}{H}\right)\left[1+\alpha\left(\frac{Y/H}{y_c}-1\right)^2\right], \quad (3)$$

where $\kappa(=0.40)$ represents the von Karman constant, H signifies the total flow depth (m), $y_c(=1/(1+\lambda^n))$ denotes the critical position of the turbulent diffusion coefficient, where $n=5/6$ and $\lambda(=U_{*I}/U_{*B})$ stands for a dimensionless parameter. Here, U_{*B} and U_{*I} refer to the shear velocity of the lower bed layer and upper ice layer (m/s), respectively. Additionally, $\beta=(\lambda-\lambda^{2n})/2(1-\lambda^{2n})$ and $\alpha=(1-\lambda)/(\lambda-\lambda^{2n})$.

In consideration of the sediment settling velocity $\omega(Y)$, this study adopts the modified formulation proposed by Wang et al. [29] based on Lorentz [48], which accounts for the combined influences of the upper ice cover and the lower channel bed

boundaries, expressed as follows:

$$\omega(Y) = \frac{\omega_0(Y/H)}{(Y/H) + \sigma(D_m/H)}, \tag{4}$$

where ω_0 represents the settling velocity of sediment particles in an infinite flow field (m/s), σ stands for the dimensionless correction coefficient, and D_m denotes the median diameter of sediment particles (mm). As per Zhang et al. [49], the mathematical expression for ω_0 can be stated as follows:

$$\omega_0 = \sqrt{\left(13.95\frac{\nu_w}{D_m}\right)^2 + 1.09\frac{\gamma_s - \gamma_w}{\gamma_w}gD_m} - 13.95\frac{\nu_w}{D_m}, \tag{5}$$

where ν_w represents the kinematic viscosity of clear water (m^2/s), while γ_w and γ_s denote the specific weights of clear water and sediment, respectively (N/m^3). Additionally, g signifies the acceleration due to gravity (m/s^2).

Equation (1) is subjected to the following initial and boundary conditions. It is assumed that, initially, the flow is devoid of sediment, i.e.,

$$S(Y, T = 0) = 0. \tag{6}$$

At the ice cover, we have assumed a zero sediment-concentration boundary condition, i.e.,

$$S(Y = H, T) = 0, \quad \text{at} \quad Y = H. \tag{7}$$

At the bottom, at a reference level $Y = A$, a fixed reference concentration is prescribed as

$$S(Y = A, T) = S_A, \quad \text{at} \quad Y = A, \tag{8}$$

where A represents the reference height (m), while S_A denotes the reference concentration (mg/L).

2.2 | Description of Various Coefficients

To utilize Equation (1) for calculating concentration distribution in an ice-covered channel, one needs to ascertain the values of several coefficients: the shear velocity of the lower bed layer, U_{*B}; shear velocity of the upper ice layer, U_{*I}; the characteristic parameter λ; the correction coefficient σ; and the inverse of the turbulent Schmidt number Λ. The subsequent section delineates the detailed procedures for determining these physical coefficients.

In investigations of flow within ice-covered channels, the two-layer hypothesis is commonly employed to partition the flow beneath the floating ice covers into two pseudo-free surface flows [8, 50]. As depicted in Figure 1, these two layers correspond to the upper ice layer and the lower bed layer, with their interface positioned at the location of the maximum stream-wise velocity. The flow characteristics within each layer are predominantly influenced by the roughness properties of the ice cover and the channel bed, respectively. The relationship between the flow depth of the lower bed layer and the total flow depth can be represented as [51]

$$\frac{H}{H_B} = \frac{m_I + m_B}{m_I}. \tag{9}$$

Here, H_B represents the flow depth of the lower bed layer (m), indicating the distance from the channel bed bottom to the plane of maximum streamwise velocity. The parameters m_I and m_B are dimensionless and are associated with the roughness of the ice cover and channel bed, respectively. Tsai and Ettema [51] provide the following expressions for m_I and m_B:

$$m_I = \kappa\sqrt{\frac{8}{f_I}}, \tag{10}$$

and

$$m_B = \kappa\sqrt{\frac{8}{f_B}}, \tag{11}$$

where f_I and f_B represent the Darcy–Weisbach resistance factors for the upper ice cover and lower bed layer, respectively. Through the combination of the Chezy formula with the Manning formula, the resistance factors f_I and f_B can be derived as shown in the following equation [29]:

$$f_I = \frac{8gn_I^2}{R_I^{1/3}}, \tag{12}$$

and

$$f_B = \frac{8gn_B^2}{R_B^{1/3}}, \tag{13}$$

where n_I and n_B denote Manning's roughness coefficients pertaining to the ice cover and channel bed, respectively. Additionally, R_I and R_B represent the hydraulic radii of the upper ice layer and lower bed (m), respectively. According to Wang et al. [52], R_I and R_B are related by the following relationship:

$$R_I = R_B\sqrt{\frac{n_I^3}{n_B^3}}. \tag{14}$$

The combination of Equations (12)–(14) results in the following relationship:

$$f_I = f_B\sqrt{\frac{n_I^3}{n_B^3}}. \tag{15}$$

Therefore, by substituting Equations (10), (11), and (15) into Equation (9), Equation (9) transforms into:

$$H_B = \frac{H}{1 + (n_I/n_B)^{3/4}}. \tag{16}$$

The flow depth H_I represents the difference between the total flow depth and the flow depth of the lower bed layer. Therefore, $H_I = H - H_B$, which can be formulated as follows:

$$H_I = \frac{H}{1 + (n_B/n_I)^{3/4}}. \tag{17}$$

Considering that the flows in the upper ice layer and the lower bed layer are typically regarded as two pseudo-free-surface flows, the shear velocities U_{*I} and U_{*B} of these layers can be determined through momentum balance, akin to the approach utilized in uniform open-channel flow [7, 25]:

$$U_{*I} = \sqrt{g s_B H_I}, \tag{18}$$

and

$$U_{*B} = \sqrt{g s_B H_B}, \tag{19}$$

where s_B denotes the bed slope of the channel. Utilizing Equations (16) and (17) in conjunction with Equations (19) and (18) yields the following expressions:

$$U_{*I} = \sqrt{\frac{g s_B H}{1 + (n_B/n_I)^{3/4}}}, \tag{20}$$

and

$$U_{*B} = \sqrt{\frac{g s_B H}{1 + (n_I/n_B)^{3/4}}}. \tag{21}$$

By employing Equations (20) and (21), the dimensionless characteristic parameter λ, defined as $\lambda = U_{*I}/U_{*B}$, can be expressed as follows:

$$\lambda = \sqrt{(n_I/n_B)^{3/4}}. \tag{22}$$

Aside from the coefficients previously mentioned, both the correction coefficient σ for the sediment settling velocity and the inverse of the Schmidt number Λ are regarded as free characteristic parameters. These parameters necessitate empirical calibration to optimize the agreement with the available experimental suspended sediment concentration data.

3 | Solution Methodology

This section outlines the methodology employed for solving the current model. Initially, a semi-analytical solution is obtained using GITT. Subsequently, a numerical solution is pursued using the cell-centered finite volume method to validate the semi-analytical solution obtained. All the calculations are performed in the MATLAB environment. Prior to this, the equations of the present model have been condensed into a compact form for the sake of simplicity. Upon substituting Equations (3) and (4) into Equation (1), it reduces to the following:

$$\frac{\partial S(y,T)}{\partial T} - \frac{\partial}{\partial y}\left[\frac{1}{H}\frac{\omega_0 y}{y + \sigma y_D} S(y,T)\right] = \frac{\partial}{\partial y}\left[\frac{1}{H} 2\Lambda\kappa U_{*B}\beta y(1-y)\left\{1 + \alpha\left(\frac{y}{y_c} - 1\right)^2\right\}\frac{\partial S(y,T)}{\partial y}\right], \tag{23}$$

where $y = Y/H$ and $y_D = D_m/H$. To express the aforementioned equation in a more concise form, let us introduce the following variables.

$$V(y) = \frac{1}{H}\frac{\omega_0 y}{y + \sigma y_D}, \tag{24}$$

and

$$K(y) = \frac{1}{H} 2\Lambda\kappa U_{*B}\beta y(1-y)\left\{1 + \alpha\left(\frac{y}{y_c} - 1\right)^2\right\}. \tag{25}$$

By utilizing Equations (24) and (25) within Equation (23), one can get the following:

$$\frac{\partial S(y,T)}{\partial T} - \frac{\partial}{\partial y}[V(y)S(y,T)] = \frac{\partial}{\partial y}\left[K(y)\frac{\partial S(y,T)}{\partial y}\right]. \tag{26}$$

Additionally, the aforementioned equation can be further simplified as follows:

$$\frac{\partial S(y,T)}{\partial T} = K(y)\frac{\partial^2 S(y,T)}{\partial y^2} + \left[\frac{\partial K(y)}{\partial y} + V(y)\right]\frac{\partial S(y,T)}{\partial y} + \frac{\partial V(y)}{\partial y} S(y,T). \tag{27}$$

The initial and boundary conditions, represented by Equations (6)–(8) respectively, can be reformulated as follows:

$$S(y, T=0) = 0, \tag{28}$$

$$S(y=1, T) = 0, \quad \text{at} \quad y = 1, \tag{29}$$

and

$$S(y=a, T) = S_a, \quad \text{at} \quad y = a. \tag{30}$$

Here, S_a denotes the reference concentration at the non-dimensional reference height a, where $a(= A/H)$.

3.1 | Semi-Analytical Solution Using GITT

In order to utilize GITT [37, 38], it is imperative that the boundary conditions exhibit homogeneity, a condition that is not satisfied in Equation (30). The standard approach involves rendering it homogeneous through the following decomposition:

$$S(y,T) = U(y,T) + f(y), \tag{31}$$

wherein $f(y)$ fulfills the following differential equation:

$$0 = K(y)\frac{d^2 f(y)}{dy^2} + \left[\frac{dK(y)}{dy} + V(y)\right]\frac{df(y)}{dy} + \frac{dV(y)}{dy} f(y), \tag{32}$$

subject to the boundary conditions:

$$f(y=1) = 0, \quad \text{at} \quad y = 1, \tag{33}$$

and

$$f(y=a) = S_a, \quad \text{at} \quad y = a. \tag{34}$$

Equation (32) represents a second-order linear ODE for $f(y)$, the solution of which is contingent upon the specific functional

expressions of the turbulent diffusion coefficient, denoted as $K(y)$, and the settling velocity, $V(y)$. In the study of Wang et al. [29], a similar type of steady solution was presented, corresponding to a one-dimensional ODE with a Dirichlet boundary condition specifying the reference concentration at a given reference height.

The governing equation for $U(y,T)$ mirrors Equation (27), sharing identical boundary conditions as described in Equations (29) and (30), albeit with the right-hand side now being equated to zero for both equations. The initial condition for $U(y,T)$ is expressed as:

$$U(y,T=0) = -f(y). \tag{35}$$

The function $U(y,T)$ is defined over the interval $y \in [a,1]$. To facilitate mathematical derivation, the spatial domain is stretched through the following mapping:

$$z = \frac{y-a}{1-a}. \tag{36}$$

As a consequence of this mapping, the domain of y is transformed to [0,1]. Consequently, the governing equation for $U(y,T)$ is altered to

$$\begin{aligned}\frac{\partial U(z,T)}{\partial T} &= \frac{K(z)}{(1-a)^2}\frac{\partial^2 U(z,T)}{\partial z^2} \\ &+ \left[\frac{1}{1-a}\frac{\partial K(z)}{\partial z} + V(z)\right]\frac{1}{1-a}\frac{\partial U(z,T)}{\partial z} \\ &+ \frac{1}{1-a}\frac{\partial V(z)}{\partial z}U(z,T),\end{aligned} \tag{37}$$

with the boundary conditions

$$U(z=1,T) = 0, \quad \text{at} \quad z=1, \tag{38}$$

and

$$U(z=a,T) = 0, \quad \text{at} \quad z=0. \tag{39}$$

To address the current problem outlined in Equation (37) using GITT, it is necessary to employ a pair of transforms, namely an integral transform. For this particular problem, we opt for a specific auxiliary problem due to its simplicity, which facilitates the construction of the required pair of transforms [37, 38]:

$$\frac{d^2\psi_n(z)}{dz^2} + \beta_n^2\psi_n(z) = 0, \quad \text{in} \quad 0 \le z \le 1, \tag{40}$$

with the boundary conditions

$$\psi_n(z) = 0, \quad \text{at} \quad z=1, \tag{41}$$

and

$$\psi_n(z) = 0, \quad \text{at} \quad z=0, \tag{42}$$

where β_n denotes the n^{th} eigenvalue, while $\psi_n(z)$ represents the corresponding eigenfunction. With this boundary constraint, the auxiliary problem defined by Equation (40) admits the following eigenfunction:

$$\psi_n(z) = \frac{\sin(\beta_n z)}{\sqrt{N_n}}, \tag{43}$$

where the normalization factor is defined as $N_n = 1/2$. The eigen values are $\beta_n = n\pi$.

An essential property of the eigen system defined previously is orthogonality, which is expressed as:

$$\int_0^1 \psi_n(z)\psi_m(z)\,dz = \begin{cases} 0, & \text{if } n \ne m, \\ 1, & \text{if } n = m. \end{cases} \tag{44}$$

With the eigenfunctions of the system established, we proceed to formulate the forward transform as:

$$\bar{S}_n(T) = \int_0^1 U(z,T)\psi_n(z)dz, \tag{45}$$

along with its corresponding inverse transform:

$$U(z,T) = \sum_{n=1}^{\infty} \bar{S}_n(T)\psi_n(z). \tag{46}$$

From a computational perspective, the inverse transform is truncated at its N-th term, with N chosen sufficiently large to achieve the desired level of accuracy. Substituting Equation (46) into Equation (37) yields

$$\begin{aligned}\sum_{n=1}^{\infty}\frac{d\bar{S}_n(T)}{dT}\psi_n(z) &= \sum_{n=1}^{\infty}\frac{K(z)}{(1-a)^2}\bar{S}_n(T)\frac{d^2\psi_n(z)}{dz^2} \\ &+ \left[\frac{1}{1-a}\frac{\partial K(z)}{\partial z} + V(z)\right]\frac{1}{1-a}\sum_{n=1}^{\infty}\bar{S}_n(T)\frac{d\psi_n(z)}{dz} \\ &+ \frac{1}{1-a}\frac{\partial V(z)}{\partial z}\sum_{n=1}^{\infty}\bar{S}_n(T)\psi_n(z).\end{aligned} \tag{47}$$

Integrating both sides of the above equation within the domain (0,1) and leveraging the property $\frac{d^2\psi_n(z)}{dz^2} = -\beta_n^2\psi_n(z)$, one can derive the ensuing system of ordinary differential equations:

$$\begin{aligned}&\sum_{n=1}^{\infty}\frac{d\bar{S}_n(T)}{dT}\int_0^1 \psi_n(z)\,\psi_m(z)dz \\ &= -\sum_{n=1}^{\infty}\bar{S}_n(T)\beta_n^2\int_0^1\frac{K(z)}{(1-a)^2}\psi_n(z)\psi_m(z)dz \\ &+ \sum_{n=1}^{\infty}\bar{S}_n(T)\int_0^1\left[\frac{1}{1-a}\frac{\partial K(z)}{\partial z} + V(z)\right]\frac{1}{1-a}\frac{d\psi_n(z)}{dz}\psi_m(z)dz \\ &+ \sum_{n=1}^{\infty}\bar{S}_n(T)\int_0^1\frac{1}{1-a}\frac{\partial V(z)}{\partial z}\psi_n(z)\psi_m(z)dz, \\ &\text{for} \quad m = 1,2,3,\ldots.\end{aligned} \tag{48}$$

Likewise, the initial condition for $U(z,T)$ can be transformed to

$$\bar{S}_m(0) = \int_0^1 [0 - f(z)]\psi_m(z)dz, \quad \text{for} \quad m = 1,2,3,\ldots. \tag{49}$$

The system of ODEs along with the initial condition can be expressed in matrix form as

$$\boldsymbol{A}\frac{d\boldsymbol{S}(T)}{dT} = \boldsymbol{G}\boldsymbol{S}(T), \quad \boldsymbol{S}(T=0) = \boldsymbol{S}_0, \tag{50}$$

where the vectors $\boldsymbol{S}(T) = \bar{S}_m(T)$ and $\boldsymbol{S}_0(T) = \bar{S}_m(0)$, and the matrix $\boldsymbol{A}$ represents an identity matrix owing to the orthonormality of the eigenvectors. The matrix $\boldsymbol{G} = \{g_{mn}\}$ is defined as

$$\begin{aligned} g_{mn} = &-\beta_n^2 \int_0^1 \frac{K(z)}{(1-a)^2}\psi_n(z)\psi_m(z)dz \\ &+ \int_0^1 \left\{\frac{1}{1-a}\frac{\partial K(z)}{\partial z} + V(z)\right\}\frac{1}{1-a}\frac{d\psi_n(z)}{dz}\psi_m(z)dz \\ &+ \int_0^1 \frac{1}{1-a}\frac{\partial V(z)}{\partial z}\psi_n(z)\psi_m(z)dz. \end{aligned} \tag{51}$$

In general, to compute the matrix $\boldsymbol{G}$, one initially solves the eigenvalue problem outlined in Equations (40)–(42) to obtain the eigenvectors ψ_n and eigenvalues β_n. Subsequently, by substituting the diffusivity distribution $K(z)$ and settling velocity $V(z)$ into Equation (51) and performing integration (either analytically or numerically), each entry of the matrix can be determined. The resulting ODE system is linear and homogeneous. This initial value problem for the coupled ODE system can be effectively solved either analytically or numerically. Upon solving the set of coupled first-order differential equations described by Equation (50), the inverse formula (Equation (46)) can be invoked to compute $U(z,T)$, while Equation (31) can be utilized to compute the concentration $S(y,T)$. The detailed intermediate mathematical derivations associated with the semi-analytical solution are provided in Appendix A.

3.2 | Numerical Solution Using Cell-Centered FVM

To implement the cell-centered finite volume method (FVM), we commence by defining Equation (1) as the governing equation. The computational domain $\Omega\,(=[a,1])$ is discretized into a set of non-overlapping control volumes (or cells), denoted as $\Omega_i \subset \Omega$, where $i = 1, 2, \ldots, n_{cell}$. We have opted for a cell-centered and uniform discretization strategy for the computational domain. In this approach, the grid point or computational node for each cell is positioned at the cell center. The boundaries (or faces) of the cells are situated midway between adjacent nodes. The one-dimensional computational domain, where the governing equation is to be solved, is depicted in Figure 2. A typical nodal point is labeled as i, while its neighboring nodes in one-dimensional geometry are denoted as $i-1$ to the south and $i+1$ to the north. The south side face center of the cell is denoted by $i-1/2$, and the north side cell face center by $i+1/2$. The distances between the nodes $i-1$ and i, and between nodes i and $i+1$, are denoted by Δy. Similarly, the distances between the face center $i-1/2$ and point i, and between i and face center $i+1/2$, are represented by $(\Delta y)/2$. The cell size is determined as $\Delta y = (1-a)/n_{cell}$. The detailed discretization procedure is provided in Appendix B.

4 | Results and Discussion

This section is structured as follows: First, the derived semi-analytical solution using GITT is validated against the cell-centered finite volume method. Next, the influence of various hydraulic parameters on the suspended concentration profile within the ice-covered channel is examined, both theoretically and visually. This is followed by a comparison between the proposed solution and available experimental data, accompanied by a comprehensive analysis to evaluate its predictive accuracy against the measurements. A sensitivity analysis of key sediment transport parameters is then conducted to assess their impact on model performance. Finally, the theoretical and practical significance of the present work is discussed.

4.1 | Validation of Semi-Analytical Solution Against FVM Solution

This section presents the numerical validation of the semi-analytical solution derived in Section 3.1. The FVM solution, discussed in Section 3.2, is utilized as a benchmark. The parameter values used are chosen from the work of Sayre and Song [8], which are $H = 0.122\,\text{m}$, $n_I = 0.0108$, $n_B = 0.0306$, $\Lambda = 6.6$, $s_B = 0.00204$, $D_m = 0.25\,\text{mm}$, $\gamma_s = 26000\,\text{N/m}^3$, $\gamma_w = 9800\,\text{N/m}^3$, $\sigma = 1.3, a = 0.0334$, and $S_a = 150\,\text{mg/L}$. For comparison purposes, Figure 3 shows the vertical concentration magnitudes at different times: $T = 0.5$, 1, 1.5, 2, 3, and 5 s. According to Figure 3, the semi-analytical solution derived using the GITT shows an excellent match with the numerical solution obtained using FVM. Furthermore, it can be observed that the concentration magnitude decreases with increasing vertical height, eventually reaching zero at the ice cover. This decline in concentration at the top is attributed to the type of sediment diffusion coefficient used in the study, which diminishes at the upper boundary. To quantify the accuracy of the GITT solution, the L^1 error and L^2 error in the semi-analytical solutions for estimating the sediment concentration magnitude were calculated [53]. These errors are normalized with the total sum of absolute values obtained from the numerical solution using FVM and are given by

$$L^1 = \frac{\sum_{i=1}^{n_{cell}} |S_{FVM,i} - S_{GITT,i}|}{\sum_{i=1}^{n_{cell}} S_{FVM,i}},$$

and

$$L^2 = \frac{\sqrt{\sum_{i=1}^{n_{cell}} (S_{FVM,i} - S_{GITT,i})^2}}{\sum_{i=1}^{n_{cell}} S_{FVM,i}}.$$

The calculated L^1 error and L^2 error at different times—$T = 0.5$ s, $T = 1$ s, $T = 1.5$ s, $T = 2$ s, $T = 3$ s, and $T = 5$ s—are tabulated in Table 1.This quantification demonstrates the accuracy of the GITT solution relative to the FVM solutions. The low error values indicate that the GITT accurately predicts the results obtained from the FVM. It is pertinent to mention that the agreement between the semi-analytical GITT solution and the numerical FVM solution demonstrates the internal consistency of the present methodology. This comparison alone does not constitute independent validation, as both methods

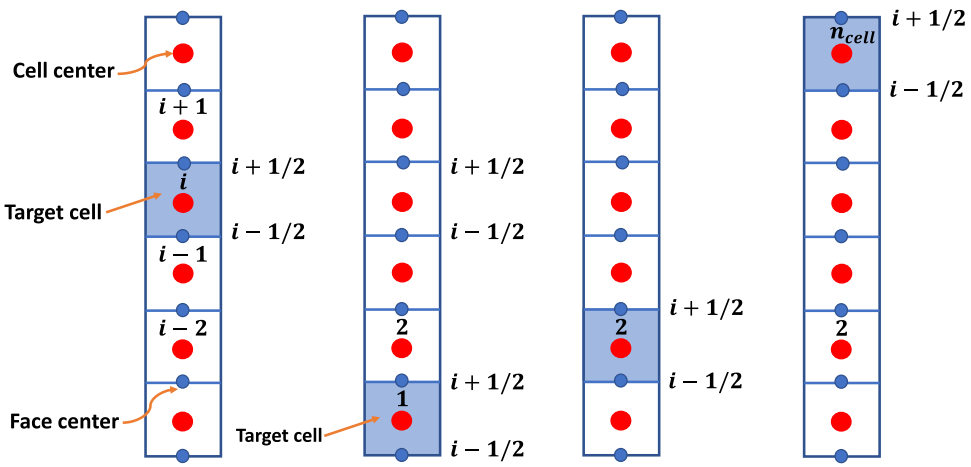

FIGURE 2 | Schematic representation of the cell arrangement in an 1D geometry.

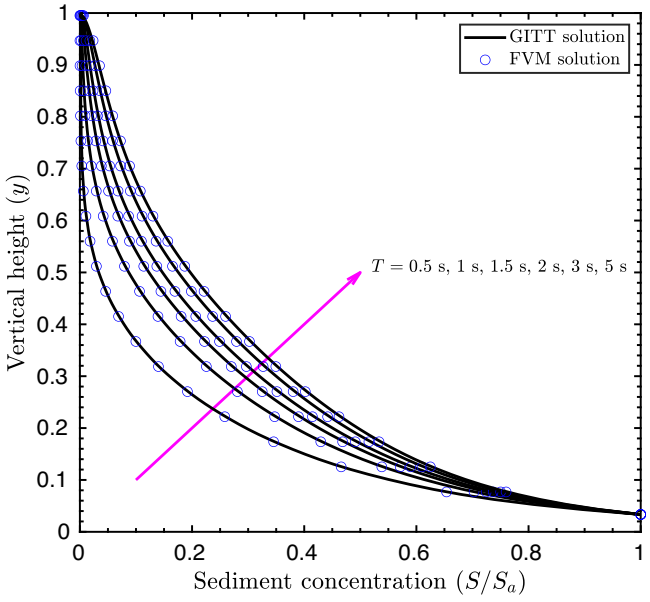

FIGURE 3 | Comparison of solutions based on GITT and FVM at different time steps.

solve the same governing equations. However, the GITT solution has also been compared against experimental measurements (Section 4.3), providing independent validation of the model and confirming that it captures the physical behavior of the system with a satisfactory level of accuracy.

Additionally, to assess the numerical robustness and grid independence of the FVM solution, a systematic grid convergence test was performed. The model was solved for four progressively refined grids with $n_{\text{cell}} = 10, 20, 50$, and 100. The concentration profiles at $T = 5$ s, obtained from successive grid refinements, were interpolated onto a common reference grid, and the relative L_2 error norm was computed as:

$$E_{L_2}^{FVM} = \sqrt{\frac{\sum_{i=1}^{N_{ip}^{FVM}} \left(S_{fine,i} - S_{coarse,i}\right)^2}{\sum_{i=1}^{N_{ip}^{FVM}} \left(S_{fine,i}\right)^2}},$$

TABLE 1 | Error table comparing GITT solution with FVM solution.

	Error quantification	
Time	L^1	L^2
0.5 s	0.009174	0.001105
1 s	0.010248	0.001075
1.5 s	0.010439	0.001089
2 s	0.010281	0.001097
3 s	0.008971	0.001015
5 s	0.006728	0.000787

where $S_{fine,i}$ and $S_{coarse,i}$ denote the solutions on the fine and coarse grids, respectively, and N_{ip}^{FVM} is the number of interpolated points.

The obtained relative errors were 1.92×10^{-2}, 9.52×10^{-3}, and 3.62×10^{-3} for the grid pairs (10, 20), (20, 50), and (50, 100), respectively. The consistent and monotonic reduction in error with grid refinement clearly demonstrates numerical convergence. At $n_{\text{cell}} = 100$, the error becomes negligible, indicating that the solution is grid-independent and numerically stable.

Similarly, the concentration profiles at $T = 5$ s were computed for different truncation numbers $N = 5, 10, 15, 30$ in the GITT solution. The profiles were interpolated onto a common reference grid, and the relative L_2 error between successive truncation numbers was calculated as:

$$E_{L_2}^{GITT} = \frac{\sqrt{\sum_{i=1}^{N_{ip}^{GITT}} \left(S_i^{(n+1)} - S_i^{(n)}\right)^2}}{\sqrt{\sum_{i=1}^{N_{ip}^{GITT}} \left(S_i^{(n+1)}\right)^2}},$$

where $S_i^{(n)}$ and $S_i^{(n+1)}$ represent the concentration at the i-th grid point for two successive truncation numbers $N^{(n)}$ and $N^{(n+1)}$.

The computed relative errors are 1.316×10^{-3} for $N = 5$ vs. 10, 2.307×10^{-3} for $N = 10$ vs. 15, and 7.730×10^{-4} for $N = 15$ vs. 30.

These results indicate that the solution is essentially converged for $N \geq 15$, confirming the robustness and reliability of the GITT solution with respect to truncation order.

4.2 | Influence of Different Hydraulic Parameters and Physical Interpretation

In this section, we investigate the influence of various hydraulic parameters on the temporal evolution of suspended sediment concentration profiles. This analysis involves calculating concentration magnitudes using Equations (27)–(30) and employing the GITT solution methodology. We then assess how different hydraulic components affect our model and explore how predicted characteristics of concentration profiles can help rationalize the phenomenon of suspended sediment transport in turbulent flow within an ice channel, as observed in reality. The hydraulic components that play a significant role in the mathematical modeling discussed in Section 2 are the ratio of shear velocities at the lower bed layer and upper ice layer, λ; the correction coefficient in settling velocity, σ; the inverse of the turbulent Schmidt number, Λ; and the particle diameter, D_m. To quantify the impacts of these individual components, we systematically vary the value of each parameter while keeping the others constant. To facilitate this context, we randomly select an experimental run from Section 4.3 to obtain the values of all parameters necessary for computing concentration profiles from Equations (27)–(30).

The effect of the dimensionless correction coefficient, σ, on the present model is illustrated in Figures 4 and 5. Figure 4 depicts the vertical concentration profiles at time intervals of $T = 1$ s and $T = 5$ s for six distinct values of σ: 1, 2, 8, 12, 16, and 20. Meanwhile, Figure 5 displays the concentration contours in the Ty-plane for three different values of σ: 1, 8, and 20. For both figures, the parameters are set to $H = 0.122$ m, $n_I = 0.0108$, $n_B = 0.0306$, $\Lambda = 6.6$, $s_B = 0.00204$, $D_m = 0.25$ mm, $\gamma_s = 26000\,\mathrm{N/m^3}$, $\gamma_w = 9800\,\mathrm{N/m^3}$, $a = 0.0334$, $S_a = 150$ mg/L.
From Figures 4 and 5, it can be observed that as σ increases, the magnitude of the vertical concentration profile also increases at a given time. As time progresses, the differences in magnitude between profiles for different σ values become more pronounced. Initially, the ice channel is free of sediment, and sediment is introduced into the suspension region only from the channel bed. As time passes, more sediment particles become suspended in the region due to turbulent diffusion, leading to an overall increase in concentration magnitude and an amplified difference between the concentration magnitudes for different σ values. Additionally, Figure 4 indicates that when σ values are close to each other, such as $\sigma = 1$ and $\sigma = 2$, the difference in concentration magnitudes is smaller compared to profiles for σ values that are further apart, such as $\sigma = 8$ and $\sigma = 20$. Upon examining Equation (4), it is evident that as σ increases, the value of the downward settling velocity ω decreases. This means the rate at which suspended sediment particles settle towards the bed decreases, allowing more sediment particles to accumulate in the suspension region. Consequently, the vertical concentration profile increases. A detailed observation of Figure 5a–c reveals that, as the value of σ increases, the contour lines gradually shift upward. Specifically, as σ increases from 1 to 20, the vertical position of contour lines corresponding to the same concentration values shows a small upward shift. For instance, at $T = 5$, in Figure 5a ($\sigma = 1$), the contour line for a concentration value of 0.09 is located at $y = 0.7006931$, and the contour line for a concentration value of 0.90 is at $y = 0.047177$. In Figure 5b ($\sigma = 8$), these vertical positions shift to $y = 0.735052$ and $y = 0.0518841$, respectively. Similarly, in Figure 5c ($\sigma = 20$), the positions shift further upward to $y = 0.77763$ and $y = 0.05965$, respectively. This upward shift is attributed to the increase in the overall concentration magnitude within the suspension region. Physically, the parameter σ serves as a correction coefficient that modulates the effective settling velocity by accounting for boundary-induced resistance from both the ice cover and the channel bed. A higher σ value reduces the influence of gravitational settling, thereby extending the suspension lifetime of sediment particles. This behavior reflects the complex interplay between the modified local hydrodynamic resistance and sediment–boundary interactions under confined ice-covered conditions. Thus, σ not only adjusts the settling dynamics but also indirectly governs the vertical distribution of sediment concentration through its coupling with the boundary geometry and turbulence structure.

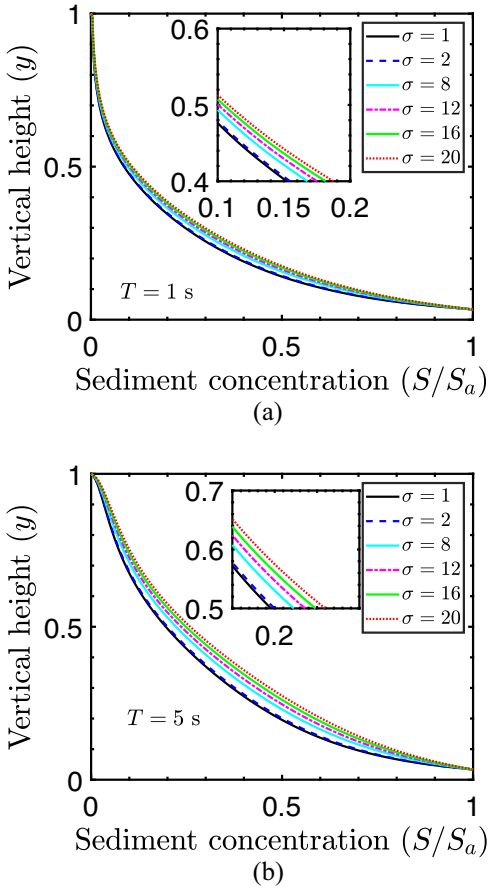

FIGURE 4 | Influence of σ on vertical concentration profiles at various time points: (a) $T = 1$ s and (b) $T = 5$ s.

Figures 6 and 7 illustrate the impact of the inverse of the Schmidt number, denoted as Λ, on the concentration distribution within turbulent flow in an ice channel. Specifically, in Figure 6, the concentration profiles are examined vertically for various values of Λ at two distinct time steps, namely $T = 1$ s and $T = 5$ s. The parameters utilized here are $H = 0.122$ m, $n_I =$

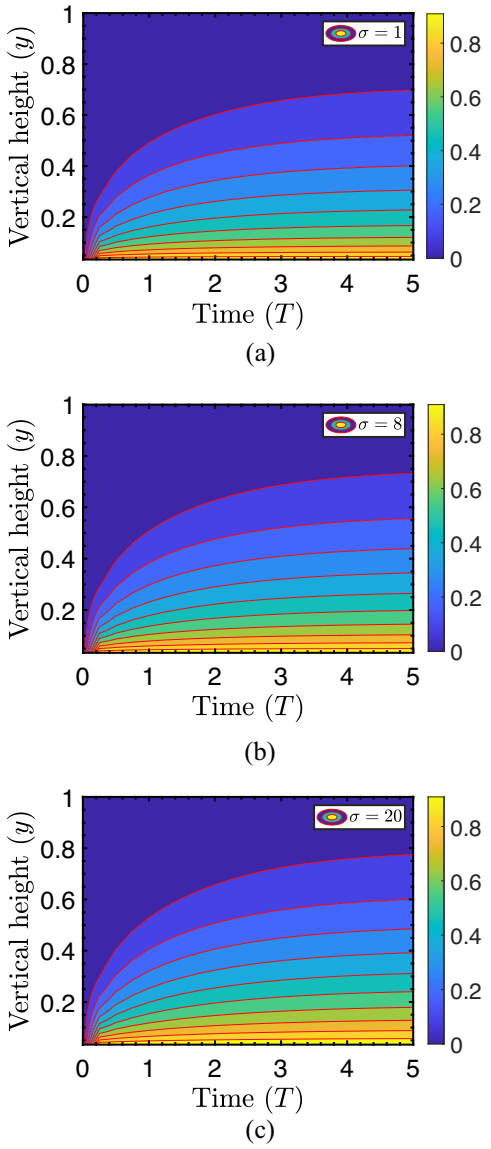

FIGURE 5 | Influence of σ on concentration contours in $Ty-$ plane. Here, (a), (b), and (c) correspond to $\sigma = 1$, 8, and 20, respectively.

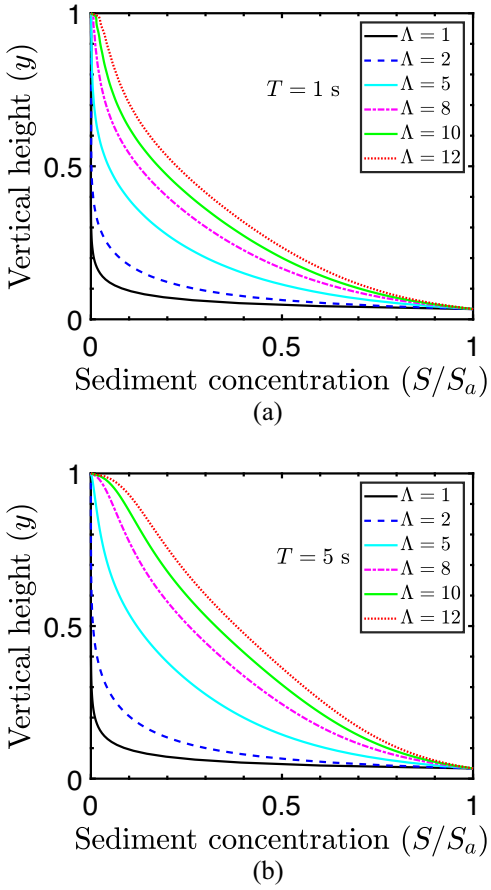

FIGURE 6 | Influence of Λ on vertical concentration profiles at various time points: (a) $T = 1$ s and (b) $T = 5$ s.

0.0108, $n_B = 0.0306$, $\sigma = 1.3$, $s_B = 0.00204$, $D_m = 0.25$ mm, $\gamma_s = 26000\,\mathrm{N/m^3}$, $\gamma_w = 9800\,\mathrm{N/m^3}$, $a = 0.0334$, $S_a = 150\,\mathrm{mg/L}$. This analysis reveals that as Λ increases, the concentration magnitude also rises at any given time. This phenomenon stems from the heightened dimensionless proportionality constant Λ, resulting in an increased turbulent diffusion coefficient. Consequently, when the turbulent diffusion coefficient, particularly with a relatively large Λ, surpasses the gravitational effect significantly, more sediment particles become readily suspended within the water column. In essence, fluid elements exhibit greater mixing across concentration gradients, thereby enhancing mass transfer rates. With increasing Λ, the capacity of turbulence to mix and transport sediment particles amplifies. This augmented mixing leads to elevated sediment concentration within the suspension region, as sediment particles are more effectively kept in suspension rather than settling out. Consequently, the vertical concentration distribution escalates at a specific time T with the rising Λ. It is noteworthy that for very small values of Λ, such as 1, the concentration magnitudes are notably lower compared to larger Λ values, such as $\Lambda = 8$, 10, and 12. Physically, Λ, being the inverse of the turbulent Schmidt number, quantifies how effectively turbulence transports sediment relative to viscous momentum diffusion. Rather than simply increasing vertical diffusion, higher Λ enhances the penetration of turbulent eddies into boundary layers near the bed and the ice cover, promoting sediment entrainment from the bed and facilitating redistribution in upper layers. This parameter thus governs the balance between turbulence-driven mixing and gravitational settling, influencing not just the magnitude but also the vertical structure of the concentration profile. Lower Λ values correspond to weaker turbulence relative to sediment settling, limiting vertical mixing and reducing suspension efficiency.

Figures 8 and 9 how the hydraulic parameter λ influences the temporal evolution of sediment concentration across six different values: $\lambda = 0.9, 1.1, 1.3, 1.5, 1.7$, and 1.9. With fixed parameters $H = 0.122\,\mathrm{m}, \sigma = 1.3$, $\Lambda = 6.6$, $s_B = 0.00204$, $D_m = 0.25$ mm, $\gamma_s = 26000\,\mathrm{N/m^3}$, $\gamma_w = 9800\,\mathrm{N/m^3}$, $a = 0.0334$, $S_a = 150\,\mathrm{mg/L}$, Figure 8 illustrates that, for a constant time interval, the vertical concentration distribution declines as λ increases. Equation (22) reveals that λ correlates with the roughness of both the ice cover and channel bed. A rise in λ implies rougher ice cover or a smoother channel bed, leading to decreased sediment suspension and consequent concentration diminishment. Notably, the decline in suspended concentration accelerates with higher λ values as time progresses, aligning with findings

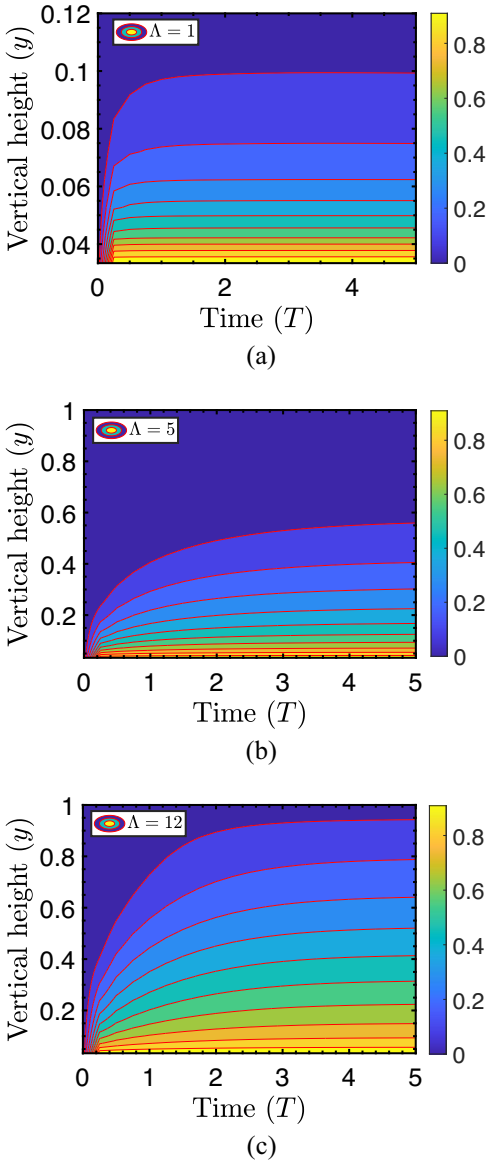

FIGURE 7 | Influence of Λ on concentration contours in $Ty-$ plane. Here, (a), (b), and (c) correspond to $\Lambda = 1$, 5, and 12, respectively.

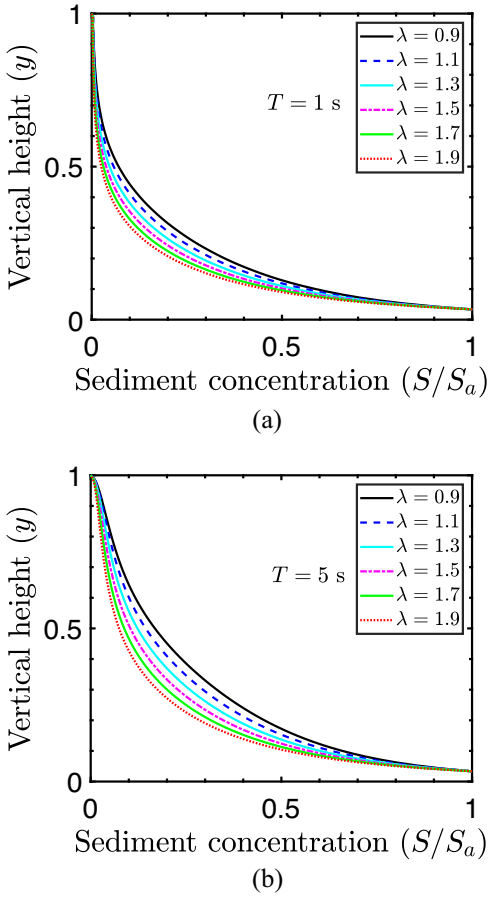

FIGURE 8 | Influence of λ on vertical concentration profiles at various time points: (a) $T = 1$ s and (b) $T = 5$ s.

by Sahu et al. [32]. Physically, λ, defined as the ratio of shear velocities between the upper ice layer and the lower bed layer, controls the vertical distribution of turbulence within the flow. Higher λ values enhance shear and turbulent intensity in the upper layer while diminishing turbulence near the bed, altering sediment transport pathways. This results in reduced entrainment of particles from the bed and a shift of mixing toward the upper water column. Lower λ values, in contrast, concentrate turbulence near the bed, favoring stronger sediment lifting and redistribution in the lower portion of the flow.

Additionally, the impact of another crucial characteristic parameter, particle diameter D_m, on concentration distribution at a specific time $T = 5$ s, has been examined. Figure 10 showcases vertical concentration profiles of suspended sediment particles for five distinct particle diameters: $D_m = 0.10$, 0.12, 0.15, 0.20, and 0.25 mm, at $T = 5$ s, with $H = 0.122$ m, $n_I = 0.0108$, $n_B = 0.0306$, $\Lambda = 6.6$, $\sigma = 1.3$, $s_B = 0.00204$, $\gamma_s = 26000\,\mathrm{N/m^3}$, $\gamma_w = 9800\,\mathrm{N/m^3}$, $a = 0.0334$, and $S_a = 150\,\mathrm{mg/L}$. It is evident that concentration magnitude rises as D_m decreases. Smaller particles, with reduced size and weight, are more prone to entraining in the suspension region, hence increasing concentration. Physically, D_m acts as a key control parameter governing the competition between inertial settling and turbulent entrainment. Larger particles possess greater inertia, making them less responsive to turbulent eddies, whereas finer particles remain dynamically coupled with turbulent fluctuations. This contrast dictates how effectively sediments interact with the turbulent structures generated near the bed and beneath the ice cover. Consequently, variations in D_m not only influence overall concentration but also modify the thickness and structure of the suspension layer by altering the efficiency of vertical mixing and sediment exchange between near-bed and upper flow regions.

A comparison among Figures 4, 6, and 8 reveals that, for a given particle diameter D_m and time T, sediment diffusion effects supersede boundary roughness and settling velocity effects.

4.3 | Comparison With Experimental Dataset

As far as the author is aware, there is no experimental data in the literature related to the transport of suspended sediment within an ice channel under an unsteady one-dimensional framework.

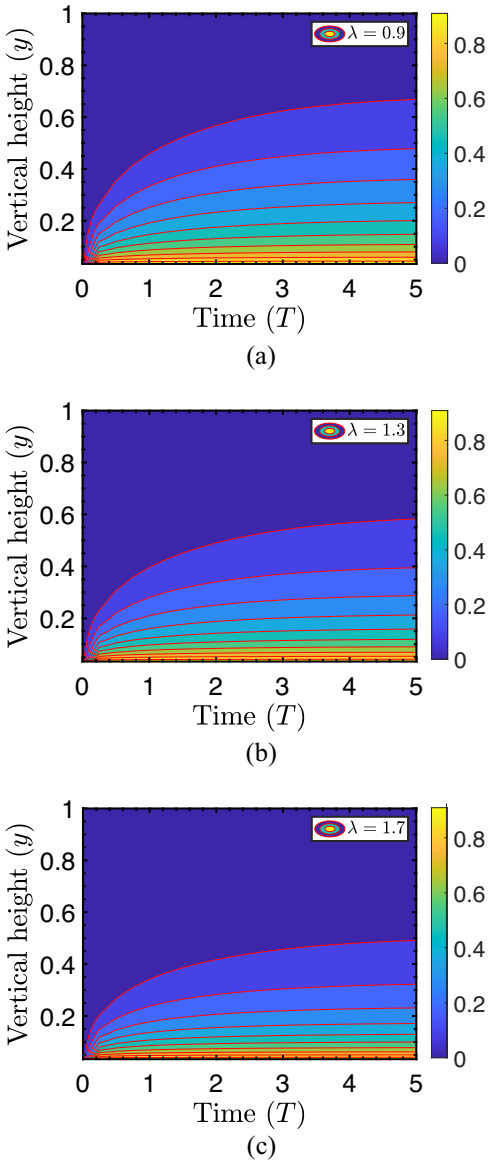

FIGURE 9 | Influence of λ on concentration contours in $Ty-$ plane. Here, (a), (b), and (c) correspond to $\lambda = 0.9, 1.3$, and 1.7, respectively.

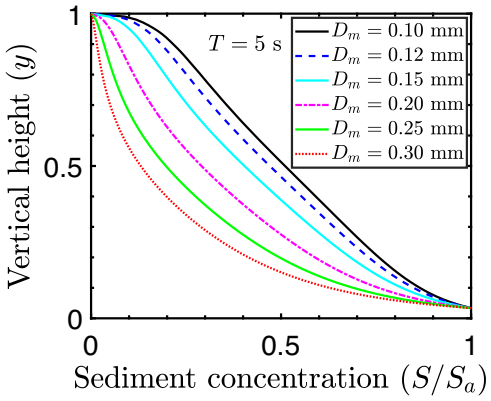

FIGURE 10 | Influence of D_m on vertical concentration profiles at a particular time.

Consequently, direct comparison of the present semi-analytical solution with experimental data is deemed unfeasible. However, available experimental literature does exist on sediment transport in ice channels under steady-state conditions. In this context, the proposed semi-analytical solution is compared to the existing experimental data, particularly over extended time periods after reaching a steady state. To achieve this, experimental data from Sayre and Song [8], Lau and Krishnappan [25], and Muste et al. [7] are taken into account. A brief summary of these experimental studies is provided herein for thoroughness and convenience.

In their research conducted in 1979, Sayre and Song [8] investigated sediment movement in a closed-loop flume equipped with a bed of sand, transparent glass walls, and an artificial ice layer simulation. The measurement portion spanned 27.4 m in length, 0.45 m in depth, and 0.914 m in width, with the flume slope adjustable without disrupting its operation. The bed comprised quartz foundry sand, possessing a geometric standard deviation of 1.41 and a median diameter of 0.25 mm. The study incorporated two types of simulated ice cover: smooth and rough. For the smooth ice cover, painted plywood panels were employed. These panels, interconnected with hinges, formed a flexible surface spanning almost the entire flume length. Each panel, measuring 1.22 m in length, 1.27 cm in thickness, and 0.91 m in width, aimed to closely replicate the conditions of natural ice cover. For the simulation of a rough ice cover, continuous masonite strips, with measurements of 0.64 cm in thickness and 2.54 cm in width, were secured beneath the panels at intervals spaced 15.24 cm apart.

Lau and Krishnappan [25] performed experiments in a rectangular flume measuring 57.3 m in length, 0.756 m in width, and 0.29 m in depth. The flume slope was adjustable through motor-driven screw jacks, while flow depth was regulated by louvered gates positioned at the downstream end. Flex-O-Lite BT10 glass beads, with a mean diameter of 0.15 mm and a specific gravity of 2.50, constituted the bed material. A 6 cm layer of these beads was evenly spread in the flume before each experiment, leveled using a screed mounted on an instrument carriage. For simulating the ice cover, 1.9 cm thick plywood with plastic laminate attached underneath was utilized, ensuring a smooth surface. These plywood panels, measuring 2.44 m in length and 0.75 m in width, were joined to form a continuous floating cover across most of the flume length. Flow depth was monitored using three-point gauges: one at each end of the test section and one mounted on an instrument carriage.

Muste et al. [7] conducted experiments utilizing a sediment-recirculating flume with dimensions of 30 m in length, 0.91 m in width, and 0.45 m in depth. This flume featured glass-sided walls to enable visual observation and the application of laser-based techniques. The flow rate measurement uncertainty was determined to be 5×10^{-5} m^3, while the slope setting resolution was approximately 5×10^{-4}. To simulate ice covers, free-floating plywood panels measuring 1.22 m in length, 0.9 m in width, and 13 mm in thickness were utilized. Considering the relatively limited length of the simulated channel, it was deemed appropriate to treat the covers as rigid. For the smooth cover condition, the bottom surface of the panels was painted, while for the rough cover condition, rectangular wooden strips measuring 12.5 mm in width, 8.5 mm in height, and 0.9 m in length were affixed to the underside surface of the panels at intervals of 50.8 mm. The

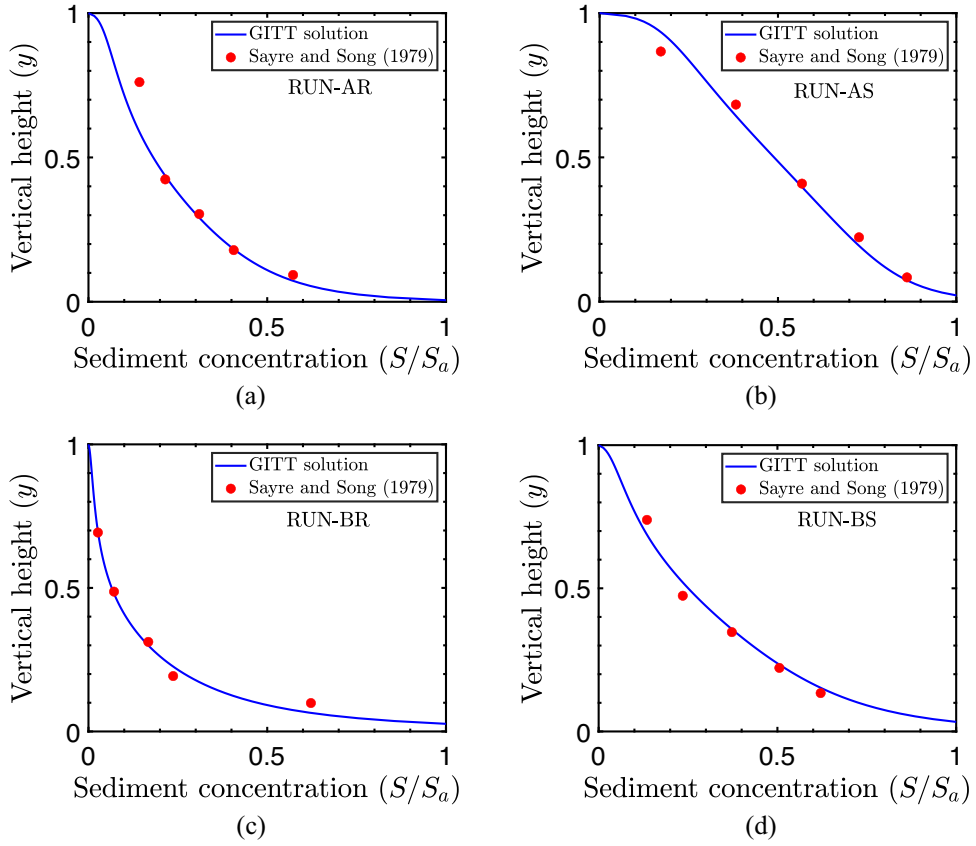

FIGURE 11 | Comparison of vertical concentration profiles obtained from the GITT solution with experimental data from Sayre and Song [8] for various runs: (a) RUN-AR, (b) RUN-AS, (c) RUN-BR, and (d) RUN-BS.

TABLE 2 | Summary of experimental data and parameter values.

toprule Reference	RUN	H (m)	n_I	n_B	s_B	D_m (mm)	γ_s(N/m^3)	γ_w(N/m^3)	Θ
Sayre and Song [8]	AR	0.121	0.0249	0.0228	0.0018	0.25	26000	9800	[10, 2]
	AS	0.118	0.0114	0.0294	0.0018	0.25	26000	9800	[24, 1]
	BR	0.148	0.0322	0.0236	0.00211	0.25	26000	9800	[4.2, 1.5]
	BS	0.122	0.0108	0.0306	0.00204	0.25	26000	9800	[7.7, 1]
Lau and Krishnappan [25]	4C	0.0877	0.009	0.0225	0.001	0.15	24500	9800	[1.7, 0.8]
	5C	0.0976	0.009	0.0225	0.001	0.15	24500	9800	[1.4, 1.4]
	7C	0.116	0.009	0.0225	0.001	0.15	24500	9800	[1.7, 2]
Muste et al. [7]	SC	0.122	0.009	0.0225	0.00015	0.25	25900	9800	[8.8, 1.3]

sediment bed consisted of a uniform fine sand with a median diameter of 0.25 mm, a geometric standard deviation of 1.4 (size range 0.075 − 0.45 mm), and a specific gravity of 2.64.

Figure 11 illustrates the comparison between the computed concentration profiles and the experimental data from Sayre and Song [8]. Figure 12a–c compare the computed concentrations with the experimental data of Lau and Krishnappan [25], while Figure 12d shows the comparison with the experimental data of Muste et al. [7]. Here, in all the figures, the dimensionless sediment concentration S/S_a has been plotted against the vertical depth, with the reference height taking the same value as that of Wang et al. [29]. Table 2 provides details of the flow and sediment characteristics for all the runs within each experimental setup. The model parameters $\Theta = [\Lambda, \sigma]$ are estimated by initially minimizing the objective function using the MATLAB function *ga*, which implements the genetic algorithm. Subsequently, the obtained model parameters are utilized as initial guesses for refining the final set of model parameters using the MATLAB function *fmincon*, which implements the interior-point algorithm.

$$\min_{\Theta} \sum_{i=1}^{n_{data}} \left[\frac{S_{exp,i} - S_{GITT,i}}{S_{exp,i}} \right]^2. \tag{52}$$

Here, n_{data} refers to the number of experimental data points for concentration in a particular RUN of the corresponding

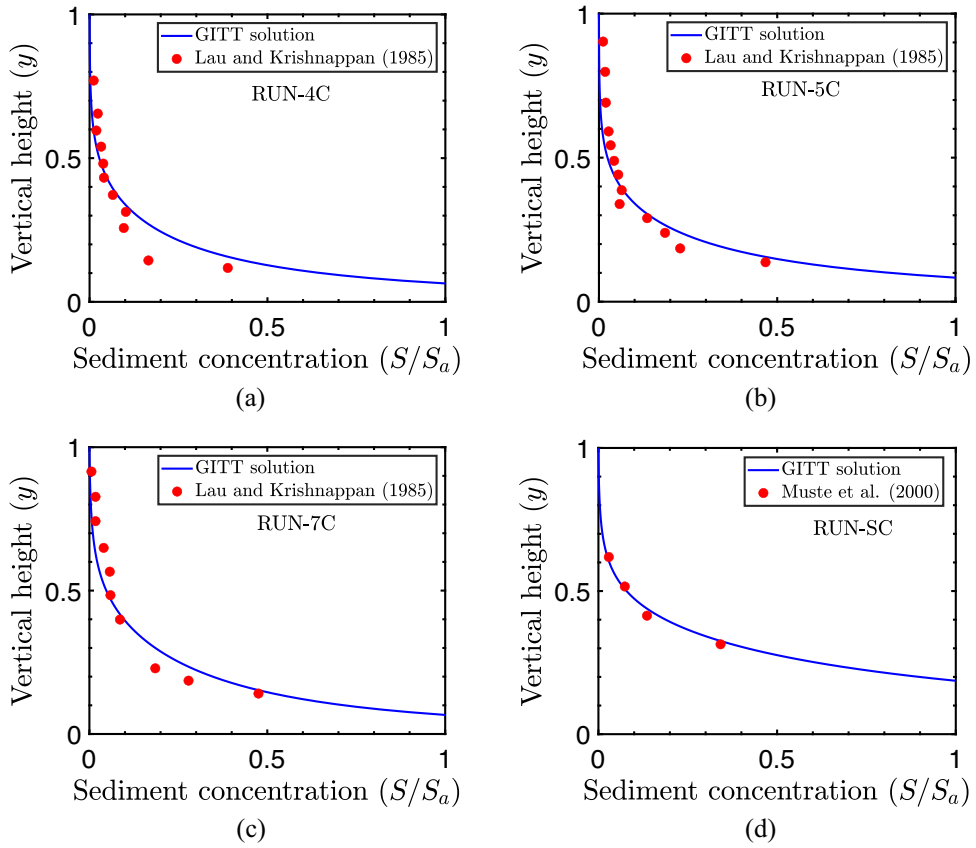

FIGURE 12 | Comparison of vertical concentration profiles obtained from the GITT solution with experimental data from Lau and Krishnappan [25] and Muste et al. [7] for various runs: (a) RUN-4C, (b) RUN-5C, (c) RUN-7C, and (d) RUN-SC.

TABLE 3 | Details of the hybrid parameter optimization used in the present study (RUN SC).

Algorithm	Parameter/Setting	Value/Description
Genetic algorithm (*ga*)	Population size	50
	Number of generations	5
	Parameter bounds	$\Lambda : [1, 10], \sigma : [1, 2]$
	Objective function	Equation (52), based on experimental vs. simulated concentrations
	Output	Optimized parameters for *fmincon* initial guess
Interior-point algorithm (*fmincon*)	Initial guess	*ga*-optimized parameters
	Parameter bounds	$\Lambda : [1, 10], \sigma : [1, 2]$
	Objective function	Equation (52), same as *ga*
	Convergence criterion	Default MATLAB interior-point tolerances

experiment. The finalized values of the optimized parameters Θ can be found in Table 2. Additionally, the algorithmic settings and parameter values used in the *ga* and *fmincon* optimization procedures are listed in Table 3 for Run SC. For all other runs, the population size and number of generations remain the same as in Run SC, except for the parameter bounds of Λ and σ. The bounds used for all runs are provided separately in Table 4.

The relationship between the model parameters Λ and σ and the underlying physical conditions, such as water temperature, sediment properties, and flow regime, is not yet fully characterized. As a consequence, the calibrated values of these parameters are dataset-specific and may differ across experimental setups or natural river conditions. The current model has been developed for steady, uniform ice-covered channel flows, and its applicability to unsteady or spatially varying flow conditions is limited. Furthermore, the calibration datasets correspond to water temperatures and flow conditions higher than those typically observed in natural ice-covered rivers. Under these circumstances, Λ and σ function as effective calibration parameters that collectively account for unresolved physical processes, including sediment settling, turbulent diffusion, and mass transfer, under the specific

TABLE 4 | Parameter bounds for Λ and σ used for the hybrid parametric optimization for all experimental runs.

RUN	AR	AS	BR	BS	4C	5C	7C	SC
Bounds (Λ, σ)	[9,10], [1,2]	[24,30], [1,2]	[1,30], [1,2]	[1,30], [1,2]	[1.65,1.7], [0.8,2]	[1,5], [1,2]	[1,1.7], [1,2]	[1,10], [1,2]

laboratory conditions. Enhancing the generalizability of the model requires additional experimental measurements under conditions more representative of natural ice-covered rivers. Such data would enable physically constrained calibration, allowing the establishment of realistic parameter ranges for Λ and σ across diverse flow and sediment regimes. While the present calibration provides a reliable representation for the experimental dataset considered, extending the model to field-scale applications will necessitate further validation and potentially refinement of the parameterization framework.

In Figures 11 and 12, the GITT solution of the present model demonstrates satisfactory agreement with the experimental data across all runs. However, in Figure 11, near the ice cover, the proposed GITT solution slightly overpredicts the concentration for RUN AS and underpredicts it for RUN AR and BS. Similar behavior has been observed in the studies by Wang et al. [29] and Sahu et al. [32]. The optimized correction coefficient for settling velocity, σ, remains around 1.3, while the values for the optimized inverse Schmidt number, Λ, range from 4.2 to 24 for all four runs by Sayre and Song [8]. In their research, Sayre and Song [8] also observed unusually large values of Λ, ranging from 1.9 to 25. They attributed these large values to inaccurate measurements of suspended sediment involving small quantities in the samples and to the possibility that the adopted terminal velocity for the sediment particle median diameter was significantly higher than the actual fall velocity of the suspended sediment particles. Nevertheless, the relatively high values of Λ observed here could be associated with the influence of the turbulent diffusion coefficient in the flow field. In Figure 12, the GITT solution demonstrates a slight underestimation compared to the measured data for RUNs 4C and 5C of Lau and Krishnappan [25] in the upper ice layer. This discrepancy bears similarity to the computed profiles for RUN AR and BS of Sayre and Song [8] in Figure 11. This likeness might be attributed to the presence of two turbulent coherent vortices beneath the ice cover, which enhance the suspended sediment concentration near the ice cover. In RUN 7C, an underestimation of the GITT solution is observed near the vertical location of zero Reynolds shear stress. This arises because the relatively high suspended sediment concentration enhances particle interactions and collisions, promoting local aggregation. Meanwhile, the near-zero Reynolds shear stress implies minimal turbulent fluctuations, leading to negligible interlayer exchange of particles. Consequently, the accumulated sediments are not easily dispersed, and under the combined effect of high SSC and weak turbulence, sediment accumulation is intensified [31]. Furthermore, the optimized average value of the turbulent Schmidt number Λ for RUN 4C, 5C, and 7C is 1.4, a value closely approximating that described in the study of Lau and Krishnappan [25]. To evaluate the accuracy of the GITT solution in predicting experimental data, we computed the L^1_{exp} and L^2_{exp}, RMSE (root mean square error), NSE (Nash–Sutcliffe efficiency), and R^2 (coefficient of determination). The mathematical expressions for those are as follows:

$$L^1_{exp} = \frac{\sum_{i=1}^{n_{data}} |S_{exp,i} - S_{GITT,i}|}{\sum_{i=1}^{n_{data}} S_{exp,i}},$$

$$L^2_{exp} = \frac{\sqrt{\sum_{i=1}^{n_{data}} (S_{exp,i} - S_{GITT,i})^2}}{\sum_{i=1}^{n_{data}} S_{exp,i}},$$

$$\text{RMSE} = \sqrt{\frac{1}{n_{data}} \sum_{i=1}^{n_{data}} (S_{GITT,i} - S_{exp,i})^2},$$

$$\text{NSE} = 1 - \frac{\sum_{i=1}^{n_{data}} (S_{GITT,i} - S_{exp,i})^2}{\sum_{i=1}^{n_{data}} (S_{exp,i} - \overline{S_{exp}})^2},$$

and

$$R^2 = \frac{\left[\sum_{i=1}^{n_{data}} (S_{GITT,i} - \overline{S_{GITT}})(S_{exp,i} - \overline{S_{exp}})\right]^2}{\sum_{i=1}^{n_{data}} (S_{GITT,i} - \overline{S_{GITT}})^2 \sum_{i=1}^{n_{data}} (S_{exp,i} - \overline{S_{exp}})^2}.$$

Here, $\overline{S_{GITT}}$ and $\overline{S_{exp}}$ denote the standard means of the corresponding predicted and experimental values. In Table 5, the determined L^1_{exp}, L^2_{exp}, RMSE, NSE, and R^2 values for all runs are presented. Typically, these errors fall within an acceptable range, but exceptions are noted for RUN 4C, 5C, and 7C. The relatively higher errors mainly result from the underestimation of suspended sediment concentration near the upper ice layer and around the vertical position corresponding to zero Reynolds shear stress. The study of Lau and Krishnappan [25] attributed these underestimated outcomes to the suspension of finer bed material fractions.

4.4 | Sensitivity Analysis of Different Parameters

In this section, sensitivity analysis is conducted to quantitatively assess the impact of the model parameters $\Theta = [\Lambda, \sigma]$ on sediment concentration magnitudes. This is achieved using variance-based sensitivity analysis (VBSA), commonly known as the Sobol' method [54, 55], a form of global sensitivity analysis. VBSA is a robust tool for understanding and quantifying the influence of input parameters on model predictions. Operating within a probabilistic framework, VBSA breaks down the output variance into contributions from individual inputs and their interactions.

To apply VBSA in this study, the output of interest is the depth-averaged concentration, $\overline{S}$, with the transport parameters $\Theta = [\Lambda, \sigma]$ serving as the model inputs. Thus, the VBSA model can be represented as:

$$\overline{S} = g^{VBSA}(\Theta). \tag{53}$$

The function $g^{VBSA}(\Theta)$ is decomposed into component functions that account for the effects of individual input parameters and their interactions. This decomposition follows the Sobol

TABLE 5 | Error table comparing GITT solution with experimental data.

Reference	RUN	Error quantification				
		L^1_{exp}	L^2_{exp}	RMSE	NSE	R^2
Sayre and Song [8]	AR	0.071703	0.043042	0.031678	0.955716	0.972732
	AS	0.049317	0.025903	0.031388	0.983572	0.989970
	BR	0.178130	0.135707	0.068219	0.896251	0.952977
	BS	0.062084	0.030254	0.025291	0.979309	0.991704
Lau and Krishnappan [25]	4C	0.615367	0.330170	0.097802	0.120425	0.882675
	5C	0.326066	0.131950	0.049101	0.842534	0.970628
	7C	0.283874	0.128528	0.049641	0.879740	0.961066
Muste et al. [7]	SC	0.126189	0.078635	0.022826	0.963621	0.992939

expansion approach [54–56]:

$$\overline{S} = g_0^{VBSA} + \sum_{i=1}^{2} g_i^{VBSA}(\Theta_i) + \sum_{1\le i<j\le 2}^{2} g_{ij}^{VBSA}(\Theta_i, \Theta_j). \quad (54)$$

Here, g_0^{VBSA} denotes the mean response of g^{VBSA} across the input space. The first-order component function, g_i^{VBSA}, reflects the independent contribution of the parameter Θ_i. Meanwhile, the subcomponent function g_{ij}^{VBSA} captures the interaction effect between the parameters Θ_i and Θ_j on g^{VBSA}. The vanishing condition implies that the integral of a Sobol expansion component function with respect to any of its variables is zero [56], i.e.,

$$\int f_m(\Theta_m) g_{ij}^{VBSA}(\Theta_i, \Theta_j) d\Theta_m = 0, \quad \text{for all} \quad m \in \{i, j\}, \quad (55)$$

where $f_m(\Theta_m)$ denotes the probability density function (PDF of the m^{th} input parameter). Accordingly, the variance of the model, $Var(\overline{S})$, can be expressed as [55]:

$$Var(\overline{S}) = \sum_{i=1}^{2} V_i + \sum_{1\le i<j\le 2}^{2} V_{i,j}, \quad (56)$$

where V_i represents the contribution of the input parameter Θ_i to the model output variance, and V_{ij} denotes the contribution from the interactions between Θ_i and Θ_j. Their respective expressions are given by

$$V_i = Var(g_i^{VBSA}(\Theta_i)) = Var(E[\overline{S}|\Theta_i]), \quad (57)$$

and

$$V_{i,j} = Var(g_{ij}^{VBSA}(\Theta_i, \Theta_j)) = Var(E[\overline{S}|\Theta_i, \Theta_j]) - V_i - V_j. \quad (58)$$

The decomposition of sensitivity indices is subsequently achieved by normalizing against the total variance as follows:

$$\sum_{i}^{2} S_i^{Sobol} + \sum_{1\le i<j\le 2}^{2} S_{i,j}^{Sobol} = 1. \quad (59)$$

Here, S_i^{Sobol} and S_{ij}^{Sobol} denote the first and second order Sobol indices, with

$$S_i^{Sobol} = V_i / Var(\overline{S}), \quad (60)$$

and

$$S_{ij}^{Sobol} = V_{ij} / Var(\overline{S}). \quad (61)$$

High values of S_i^{Sobol} signify that the corresponding parameters have a significant impact on the output variance. In contrast, S_{ij}^{Sobol} measures the effects of interaction terms between parameters. The total sensitivity index, $S_{T_i}^{Sobol}$, is defined as follows [55]:

$$S_{T_i}^{Sobol} = S_i^{Sobol} + \sum_{j}^{2} S_{ij}^{Sobol}$$
$$= 1 - \frac{Var(E[\overline{S}|\Theta_{\sim_i}])}{Var(\overline{S})} = \frac{E[Var(\overline{S}|\Theta_{\sim_i})]}{Var(\overline{S})}. \quad (62)$$

Here, $\Theta_{\sim_i}$ represents the set of all components except Θ_i. The total sensitivity index, $S_{T_i}^{Sobol}$, captures both the main effect and all interaction effects involving Θ_i. A higher value of $S_{T_i}^{Sobol}$ indicates that Θ_i is influential, including through interactions. If there is a large difference between $S_{T_i}^{Sobol}$ and S_i^{Sobol}, it suggests that significant interaction effects involving Θ_i are present.

In all the experimental runs described in Section 4.3, the VBSA was conducted, and the results are presented in Table 6. From Table 6, it is evident that S_Λ^{Sobol} consistently shows significantly higher values compared to S_σ^{Sobol}. This indicates that Λ is generally more influential than σ in predicting suspended sediment magnitudes in ice-covered channel flows. The VBSA also highlights the importance of focusing on the values of Λ when modeling suspended sediment transport in such conditions. It is worth noting that there is limited experimental data available in the literature for ice-covered turbulent channel flows, and additional experimental data is needed for a more thorough VBSA. This VBSA represents a valuable step forward in understanding the sensitivity of parameters in ice-covered flow models.

4.5 | Theoretical Significance of the Present Research

To emphasize the significance of this research, it is crucial to delineate how the proposed model advances beyond existing analytical and semi-analytical formulations for suspended

TABLE 6 | Summary of VBSA for the chosen experimental data.

Reference	RUN	$S_{\Lambda}^{Sobol}(\%)$	$S_{\sigma}^{Sobol}(\%)$	$S_{T_{\Lambda}}^{Sobol} - S_{\Lambda}^{Sobol}(\%)$	$S_{T_{\sigma}}^{Sobol} - S_{\sigma}^{Sobol}(\%)$
Sayre and Song [8]	AR	5.34	0.55	94.11	94.12
	AS	5.12	0.04	94.84	94.85
	BR	13.95	0.03	86.03	86.01
	BS	8.92	0.02	91.06	91.06
Lau and Krishnappan [25]	4C	9.51	0.01	90.48	90.49
	5C	13.78	0.01	86.21	86.20
	7C	9.45	0.02	90.53	90.53
Muste et al. [7]	SC	9.44	0.01	90.55	90.56

sediment concentration, particularly those developed for ice-covered channel flows, while also addressing relevant studies pertaining to open-channel flow conditions. The analytical framework proposed by Wang et al. [29] predicts suspended sediment concentration in ice-covered alluvial channels. This model was grounded in a Rouse-like formulation. It also included a sensitivity analysis of various hydraulic parameters on concentration distribution. The fractional-derivative framework developed by Wang et al. [30] describes the dynamics of suspended sediment concentration. This model captured the non-local characteristics of vertical diffusion of suspended sediment particles in such channels. While both models analytically address particle-turbulence interaction in suspension, they are limited to steady-state conditions. The semi-analytical model proposed by Sahu and Ghoshal [34] represents a steady, one-dimensional coupled system of ODEs describing velocity and suspension concentration in an ice-covered channel. These models do not provide insights into the temporal evolution of concentration profiles. Additionally, their sensitivity analysis methods lack mathematical rigor. The two-dimensional analytical framework developed by Sahu et al. [32] incorporates a time-dependent term to characterize unsteady variations in suspended sediment concentration under ice-covered channel conditions. The model was solved numerically using a finite difference method. It predicts temporal evolution but is constrained by numerical approaches. It also lacks a rigorous procedure for optimizing and evaluating parameter sensitivities. The unsteady fractional advection–diffusion framework developed by Sahu et al. [33] employs the fADE to represent memory-dependent sediment transport processes. While capturing temporal dynamics, this model also relies on numerical methods. The recent analytical study by Sahu et al. [36] analyzes an unsteady, one-dimensional time-fractional advection–diffusion equation using fractional calculus, capturing memory-dependent particle transport in an ice-covered channel, in contrast to the present classical analysis. The study assumes depth-averaged, constant turbulent diffusion coefficients and depth-averaged, constant settling velocity to simplify the derivation of the analytical solution. These studies by Sahu et al. [33] and Sahu et al. [36] also do not incorporate a rigorous sensitivity analysis framework.

While Zhang et al. [46] applied PINNs to solve the 1DV suspended sediment settling-diffusion equation, and Zhang et al. [20] derived an analytical solution for unsteady, non-conservative conditions, neither study incorporates ice-cover dynamics. They assume constant vertical profiles for turbulent diffusivity and settling velocity. This assumption is appropriate for wave-dominated shallow environments. In such environments, turbulence from wind, wave breaking, and bottom friction mixes throughout the water column. As a result, the eddy diffusivity can be considered nearly uniform [20, 57]. Both studies have proven highly effective in the context of sediment transport modeling.

Although several recent analytical and semi-analytical studies have addressed suspended sediment transport under nonequilibrium conditions, the majority do not account for ice-covered flow dynamics. In some of these studies on open-channel flows, the turbulent diffusion coefficient in the advection–diffusion equation is assumed constant throughout the vertical depth. This assumption simplifies the mathematical formulation. Depending on the physical focus of the study, it may also adequately represent the intended flow conditions. As a result, the analytical or semi-analytical solution becomes more tractable. In other analytical and semi-analytical studies of suspended sediment concentration in open-channel flows, depth-dependent turbulent diffusivity and settling velocity have been incorporated to more accurately capture the vertical variation of sediment transport. For ice-covered flows, analytical/semi-analytical solutions for suspended sediment concentration are typically limited to steady-state cases [29, 30, 34], while some unsteady analytical models assume constant turbulent diffusion coefficients and settling velocities [36]. Some numerical approaches [32] account for the vertical variation of these parameters. The present GITT solution effectively accounts for both the turbulent diffusion coefficient and the sediment settling velocity as functions of the vertical coordinate. This capability arises from the relative ease of constructing integral transform pairs and performing forward and inverse transforms for analytical or semi-analytical manipulation of the present governing equations. Additionally, the present GITT solution remains applicable even when these parameters are treated as constant, providing a more generalized semi-analytical strategy for predicting suspended sediment concentration in ice-covered flows. However, for highly nonlinear equations or irregular boundary conditions, identifying suitable closed-form transform pairs can be challenging, which may limit the direct applicability of the method in such cases.

In practice, parameter selection is critical for modeling ice-covered channel flows, and accurate quantification of parameter sensitivity is essential for reliable predictions of suspended

sediment concentration. Existing models for sediment suspension in ice-covered channels, whether analytical, semi-analytical, or numerical, generally do not address parameter selection through a rigorous mathematical procedure. Additionally, numerical methods are inherently prone to errors, which, when combined with non-rigorous sensitivity analyses, can compromise the validity of physical models. The present study overcomes these limitations by integrating the present GITT framework with parameter optimization and variance-based sensitivity analysis. Parameters were optimized using a mathematically precise approach. This approach combined genetic algorithms with the interior point algorithm. A robust sensitivity analysis was conducted using Sobol's variance-based method. This method provided detailed quantification of sensitivity indices.

The present semi-analytical GITT framework further distinguishes itself from purely data-driven approaches by explicitly incorporating key physical processes, such as turbulence-induced vertical variations in diffusion and settling velocity. This allows the method to produce reliable predictions even when experimental or field data are limited, while also enabling systematic sensitivity analysis and parametric studies.

By integrating parameter optimization and variance-based sensitivity analysis within the GITT framework, the present solution not only serves as a benchmark for validating numerical and data-driven models but also provides deeper insight into the dominant physical mechanisms governing suspended sediment transport in ice-covered channel flows.

4.6 | Practical Significance of the Present Research

The semi-analytical GITT solution presented here provides accurate, time-dependent vertical profiles of suspended sediment in ice-covered channels, supporting hydraulic engineering and environmental management. It can enable prediction of suspended load and, consequently, help understand sediment accumulation and scouring near ice-covered beds, informing the design and maintenance of hydraulic structures such as bridges and intakes. Sensitivity analysis of parameters, including settling velocity and turbulent Schmidt number, allows assessment of sediment transport under varying ice and flow conditions and can facilitate adaptive strategies in climate-affected regions. The methodology may also be extended to contaminants or microplastics, supporting water quality management. Additionally, the semi-analytical solution serves as a benchmark for testing and validating numerical sediment transport models in ice-covered channels, ensuring that large-scale hydraulic simulations used for infrastructure design or environmental assessments remain robust and reliable.

5 | Conclusions

This study presents a semi-analytical solution based on GITT to predict suspended particle concentration profiles in ice-covered turbulent channel flows under unsteady conditions. The model incorporates a comprehensive turbulent diffusion coefficient and settling velocity. It accounts for both channel bed and ice surface roughness. Validation is performed against experimental data and numerical methods. The results demonstrate high accuracy. This provides a valuable tool for sediment transport analysis in such environments. The key findings of this study are summarized as follows:

- As the correction coefficient in settling velocity (σ) increases, the magnitude of the vertical concentration profile also increases at a given time. Over time, the differences in the magnitude of profiles corresponding to various σ values become more pronounced.
- The vertical concentration distribution at a specific time (T) increases with the rising inverse of the Schmidt number (Λ). For very small values of Λ, the concentration magnitudes are significantly lower compared to larger Λ values.
- An increase in the roughness of ice cover or the smoothness of the channel bed results in reduced sediment suspension and a consequent decline in concentration. This reduction in suspended concentration becomes more pronounced with higher λ values as time progresses.
- An optimal set of model parameters, including the turbulent Schmidt number and the settling velocity correction coefficient, has been identified for several experimental datasets. Statistical indices such as L_1, L_2, RMSE, NSE, and R^2 indicate that the errors quantified with these optimized parameters fall within an acceptable range when comparing the GITT solution to experimental data.
- The VBSA highlights the inverse of the turbulent Schmidt number as the most sensitive parameter in predicting concentration profiles in ice-covered channels. This sensitivity is quantified using various Sobol indices.
- The derived GITT solution serves as a benchmark for validating numerical solutions in the context of sediment-laden, ice-covered channel flows.

In the future, one may include parameters such as unsteady velocity profiles. Non-uniform streamwise sediment concentrations can also be added to the current model. These additions would enhance the efficacy of concentration prediction in an ice-covered channel. Although this study primarily addresses suspended sediment particles, the methodology is not limited to this particulate matter. The proposed semi-analytical solution utilizing GITT holds broader potential. It can be extended to model the concentration of various suspended substances within the ice-covered channel. This includes contaminants released from the upper ice layer. It also applies to the transport parameters of microplastics.

A key limitation of the present study is the lack of direct unsteady experimental data under ice-covered flow conditions. Consequently, the model validation was restricted to steady-state datasets available in the literature. Although these comparisons provide qualitative confidence in the model's performance, they cannot fully capture the transient dynamics represented in the unsteady formulation. Future experimental studies focusing on time-resolved measurements of sediment concentration profiles under ice cover would be valuable for further model verification.

Author Contributions

Sourav Hossain: conceptualization, methodology, validation, writing – original draft. **Ashok Das:** supervision, writing – review and editing. **Sanjib Naskar:** writing – review and editing. **Sweta Narayan Sahu:** validation. **Koeli Ghoshal:** supervision, writing – review and editing.

Acknowledgments

The corresponding author acknowledges the financial assistance received from the IIT (ISM) Dhanbad through FRS Project (Project No. MISC 0090).

Conflicts of Interest

The authors declare no conflicts of interest.

Data Availability Statement

The datasets used and/or analyzed during the current study available from the corresponding author on reasonable request.

References

1. F. Wang, Z. Li, and W. Huai, "A Random Displacement Model of Sediment Transport in Ice-Covered Alluvial Channel Flows," *Environmental Science and Pollution Research* 29, no. 46 (2022): 70 099–70 113.

2. Y. L. Lau and B. G. Krishnappan, "Ice Cover Effects on Stream Flows and Mixing," *Journal of the Hydraulics Division* 107, no. 10 (1981): 1225–1242.

3. S. G. A. Zare, S. A. Moore, C. D. Rennie, O. Seidou, H. Ahmari, and J. Malenchak, "Estimation of Composite Hydraulic Resistance in ice-Covered Alluvial Streams," *Water Resources Research* 52, no. 2 (2016): 1306–1327.

4. B. Morse and F. Hicks, "Advances in River Ice Hydrology 1999–2003," *Hydrological Processes: An International Journal* 19, no. 1 (2005): 247–263.

5. A. Robert and T. Tran, "Mean and Turbulent Flow Fields in a Simulated Ice-Covered Channel With a Gravel Bed: Some Laboratory Observations," *Earth Surface Processes and Landforms* 37, no. 9 (2012): 951–956.

6. L. Wazney, S. P. Clark, J. Malenchak, I. Knack, and H. T. Shen, "Numerical Simulation of River Ice Cover Formation and Consolidation at Freeze-Up," *Cold Regions Science and Technology* 168 (2019): 102884.

7. M. Muste, F. Braileanu, and R. Ettema, "Flow and Sediment Transport Measurements in a Simulated Ice-Covered Channel," *Water Resources Research* 36, no. 9 (2000): 2711–2720.

8. W. W. Sayre and G. Song, *Effects of Ice Covers on Alluvial Channel Flow and Sediment Transport Processes*, Technical Report (Iowa Institute of Hydraulic Research, 1979).

9. T. Iida, A. Kajihara, H. Okubo, and K. Okajima, "Effect of Seasonal Snow Cover on Suspended Sediment Runoff in a Mountainous Catchment," *Journal of Hydrology* 428 (2012): 116–128.

10. L. C. van Rijn, "Sediment Transport, Part II: Suspended Load Transport," *Journal of Hydraulic Engineering* 110, no. 11 (1984): 1613–1641.

11. M. Umeyama, "Vertical Distribution of Suspended Sediment in Uniform Open-Channel Flow," *Journal of Hydraulic Engineering* 118, no. 6 (1992): 936–941.

12. B. Mazumder and K. Ghoshal, "Velocity and Concentration Profiles in Uniform Sediment-Laden Flow," *Applied Mathematical Modelling* 30, no. 2 (2006): 164–176.

13. X. Liu and M. Nayamatullah, "Semianalytical Solutions for one-Dimensional Unsteady Nonequilibrium Suspended Sediment Transport in Channels With Arbitrary Eddy Viscosity Distributions and Realistic Boundary Conditions," *Journal of Hydraulic Engineering* 140, no. 5 (2014): 04014011.

14. S. Mohan, M. Kumbhakar, K. Ghoshal, and J. Kumar, "Semianalytical Solution for Simultaneous Distribution of Fluid Velocity and Sediment Concentration in Open-Channel Flow," *Journal of Engineering Mechanics* 145, no. 11 (2019): 04019090.

15. C. Li, D. Chen, F. Ge, and Y. Chen, "Fractional Derivative Modeling for Suspended Sediment in Unsteady Flows," *Communications in Nonlinear Science and Numerical Simulation* 79 (2019): 104971.

16. S. Miyata, S. Mizugaki, S. Naito, and M. Fujita, "Application of Time Domain Reflectometry to High Suspended Sediment Concentration Measurements: Laboratory Validation and Preliminary Field Observations in a Steep Mountain Stream," *Journal of Hydrology* 585 (2020): 124747.

17. D. Pal and K. Ghoshal, "Effect of Particle Concentration on Sediment and Turbulent Diffusion Coefficients in Open-Channel Turbulent Flow," *Environmental Earth Sciences* 75 (2016): 1–11.

18. S. Hossain, G. Singh, A. Dhar, and K. Ghoshal, "Generalized non-Equilibrium Suspended Sediment Transport Model With Hindered Settling Effect for Open Channel Flows," *Journal of Hydrology* 612 (2022): 128145.

19. S. Hossain, S. Sen, K. Ghoshal, and A. Dhar, "Combined Impact of Density Stratification and Hindered Settling on Nonequilibrium Suspended Sediment Transport in Open Channel Flows," *Journal of Hydrologic Engineering* 28, no. 8 (2023): 04023023.

20. S. Zhang, Z. Zhao, J. Wu, et al., "Optimization of Suspended Particulate Transport Parameters From Measured Concentration Profiles With a new Analytical Model," *Water Research* 254 (2024): 121407.

21. S. Zhang, J. Wu, Y. Jia, Y.-G. Wang, Y. Zhang, and Q. Duan, "A Temporal Lasso Regression Model for the Emergency Forecasting of the Suspended Sediment Concentrations in Coastal Oceans: Accuracy and Interpretability," *Engineering Applications of Artificial Intelligence* 100 (2021): 104206.

22. S. Zhang, J. Wu, Y.-G. Wang, D.-S. Jeng, and G. Li, "A Physics-Informed Statistical Learning Framework for Forecasting Local Suspended Sediment Concentrations in Marine Environment," *Water Research* 218 (2022): 118518.

23. S. Zhang, Z. Zhao, G. Li, et al., "Estimation of Sediment Transport Parameters From Measured Suspended Concentration Time Series Under Waves and Currents With a New Conceptual Model," *Water Resources Research* 60, no. 4 (2024): e2023WR034933.

24. B. G. Krishnappan, "Suspended Sediment Profile for Ice-Covered Flows," *Journal of Hydraulic Engineering* 109, no. 3 (1983): 385–399.

25. Y. L. Lau and B. G. Krishnappan, "Sediment Transport Under Ice Cover," *Journal of Hydraulic Engineering* 111, no. 6 (1985): 934–950.

26. I. M. Knack, "Mathematical Modeling of River Dynamics With Thermal-Ice-Sediment Processes" (Ph.D. diss., Clarkson University, 2011).

27. F. Huang, "A Numerical Model Study on River Ice and Sediment Dynamics" (Ph.D. diss., Clarkson University, 2014).

28. I. Knack and H.-T. Shen, "Sediment Transport in Ice-Covered Channels," *International Journal of Sediment Research* 30, no. 1 (2015): 63–67.

29. F. Wang, W. Huai, and Y. Guo, "Analytical Model for the Suspended Sediment Concentration in the Ice-Covered Alluvial Channels," *Journal of Hydrology* 597 (2021): 126338.

30. F. Wang, Z. Li, Y. Zhang, and J. Guo, "Fractional Derivative Modeling for Sediment Suspension in Ice-Covered Channels," *Environmental Science and Pollution Research* 30, no. 5 (2023): 12 508–12 520.

31. W. Huai, H. Chen, Z. Yang, D. Li, and F. Wang, "Estimation of the Suspended Sediment Concentration in Ice-Covered Channels Based on the Gravitational Theory," *Journal of Hydrology* 637 (2024): 131337.

32. S. N. Sahu, S. Hossain, S. Sen, and K. Ghoshal, "Sediment Transport in Ice-Covered Channel Under Non-Equilibrium Condition," *Environmental Earth Sciences* 83 (2024): 1–15.

33. S. N. Sahu, S. Sen, S. Hossain, and K. Ghoshal, "Unsteady Suspended Sediment Distribution in an Ice-Covered Channel Through Fractional Advection–Diffusion Equation," *Journal of Engineering Mathematics* 147, no. 1 (2024): 7.

34. S. N. Sahu and K. Ghoshal, "Simultaneous Study of Sediment Concentration and Fluid Velocity in an Ice-Covered Channel," *Cold Regions Science and Technology* 241 (2025): 104655.

35. M. Khader, "On the Numerical Solutions for the Fractional Diffusion Equation," *Communications in Nonlinear Science and Numerical Simulation* 16, no. 6 (2011): 2535–2542.

36. S. N. Sahu, S. Hossain, C. Gualtieri, and K. Ghoshal, "Analytical and Numerical Investigation of Suspended Sediment Concentration Profiles in an Ice-Covered Channel Using the Time-Fractional Advection–Diffusion Equation," *Journal of Engineering Mechanics* 151, no. 9 (2025): 04025045.

37. R. M. Cotta and M. D. Mikhaylov, *Heat Conduction: Lumped Analysis, Integral Transforms, Symbolic Computation* (Wiley-Interscience, 1997).

38. R. M. Cotta, *Integral Transforms in Computational Heat and Fluid Flow* (CRC Press, 2020).

39. M. D. Mikhailov and M. N. Ozisik, *Unified Analysis and Solutions of Heat and Mass Diffusion* (John Wiley and Sons Inc., 1984).

40. X. Liu, "Analytical Solutions for Steady Two-Dimensional Suspended Sediment Transport in Channels With Arbitrary Advection Velocity and Eddy Diffusivity Distributions," *Journal of Hydraulic Research* 54, no. 4 (2016): 389–398.

41. S. Wortmann, M. T. Vilhena, D. M. Moreira, and D. Buske, "A New Analytical Approach to Simulate the Pollutant Dispersion in the PBL," *Atmospheric Environment* 39, no. 12 (2005): 2171–2178.

42. C. Costa, M. Vilhena, D. Moreira, and T. Tirabassi, "Semi-Analytical Solution of the Steady Three-Dimensional Advection-Diffusion Equation in the Planetary Boundary Layer," *Atmospheric Environment* 40, no. 29 (2006): 5659–5669.

43. D. Moreira, M. Vilhena, D. Buske, and T. Tirabassi, "The GILTT Solution of the Advection–Diffusion Equation for an Inhomogeneous and Nonstationary PBL," *Atmospheric Environment* 40, no. 17 (2006): 3186–3194.

44. D. Buske, M. Vilhena, D. Moreira, and T. Tirabassi, "An Analytical Solution of the Advection-Diffusion Equation Considering Non-Local Turbulence Closure," *Environmental Fluid Mechanics* 7 (2007): 43–54.

45. M. Cassol, S. Wortmann, and U. Rizza, "Analytic Modeling of two-Dimensional Transient Atmospheric Pollutant Dispersion by Double GITT and Laplace Transform Techniques," *Environmental Modelling & Software* 24, no. 1 (2009): 144–151.

46. S. Zhang, J. Deng, X. Li, et al., "Solving the One Dimensional Vertical Suspended Sediment Mixing Equation With Arbitrary Eddy Diffusivity Profiles Using Temporal Normalized Physics-Informed Neural Networks," *Physics of Fluids* 36, no. 1 (2024).

47. J. Guo, H. Shan, H. Xu, Y. Bai, and J. Zhang, "Exact Solution for Asymmetric Turbulent Channel Flow With Applications in Ice-Covered Rivers," *Journal of Hydraulic Engineering* 143, no. 10 (2017): 04017041.

48. H. A. Lorentz, "Ein Allgemeiner Satz, die Bewegung Einer Reibenden flüssigkeit Betreffend, Nebst Einigen Anwendungen Desselben," *Abhandlungen über Theoretische Physik* 1 (1907): 23.

49. R. Zhang, J. Xie, M. Wang, and J. Huang, *River Sediment Dynamics* (China Water and Power Press, 1998).

50. M. J. Teal, R. Ettema, and J. F. Walker, "Estimation of Mean Flow Velocity in Ice-Covered Channels," *Journal of Hydraulic Engineering* 120, no. 12 (1994): 1385–1400.

51. W.-F. Tsai and R. Ettema, "Modified Eddy Viscosity Model in Fully Developed Asymmetric Channel Flows," *Journal of Engineering Mechanics* 120, no. 4 (1994): 720–732.

52. F. Wang, W. Huai, M. Liu, and X. Fu, "Modeling Depth-Averaged Streamwise Velocity in Straight Trapezoidal Compound Channels With ice Cover," *Journal of Hydrology* 585 (2020): 124336.

53. A. Das, J. Paul, S. Heinrich, and J. Kumar, "Development and Analysis of Moments Preserving Finite Volume Schemes for Multi-Variate Nonlinear Breakage Model," *Proceedings of the Royal Society A* 479, no. 2271 (2023): 20220658.

54. I. Soboĺ, "Sensitivity Estimates for Nonlinear Mathematical Models," *Mathematical Modeling and Computational Experiment* 1 (1993): 407.

55. R. C. Smith, *Uncertainty Quantification: Theory, Implementation, and Applications*, vol. 12 (Computational Science and Engineering SIAM, 2013).

56. M. M. Opgenoord, D. L. Allaire, and K. E. Willcox, "Variance-Based Sensitivity Analysis to Support Simulation-Based Design Under Uncertainty," *Journal of Mechanical Design* 138, no. 11 (2016): 111410.

57. P. Wang, W. Yuan, and L. Min, "Measuring and Modeling Suspended Sediment Concentration Profiles in the Surf Zone," *Journal of Palaeogeography* 1, no. 2 (2012): 172–192.

58. H. K. Versteeg, *An Introduction to Computational Fluid Dynamics the Finite Volume Method, 2/E* (Pearson/Prentice Hall, Pearson Education India, 2007).

59. B. P. Leonard, "A Stable and Accurate Convective Modelling Procedure Based on Quadratic Upstream Interpolation," *Computer Methods in Applied Mechanics and Engineering* 19, no. 1 (1979): 59–98.

Appendix A: Intermediate Mathematical Derivations in GITT

This appendix presents the intermediate mathematical derivations used directly in the GITT calculations. We provide three intermediate calculations: (i) the eigenfunction calculation (Equation 43), (ii) the derivation of $f(z)$ in Equation (49), and (iii) the construction of the system of ODEs (Equation 50). Interested readers may refer to these steps for a complete, step-by-step understanding of the GITT formulation.

(i) Eigenfunction calculation (Equation 43): The general solution of the auxiliary problem (Equation 40) can be expressed as

$$\psi_n(z) = k_1 \cos(\beta_n z) + k_2 \sin(\beta_n z). \tag{A1}$$

Using the boundary condition given in Equation (42) in Equation (A1), we obtain $k_1 = 0$. Hence,

$$\psi_n(z) = k_2 \sin(\beta_n z). \tag{A2}$$

Next, by applying the other boundary condition (specified in Equation 41) to Equation (A2), we find that, for nonzero $\psi_n(z)$,

$$\beta_n = n\pi. \tag{A3}$$

Neglecting the arbitrary constant, the eigenfunction can therefore be written as

$$\Psi_n(z) = \sin(\beta_n z). \tag{A4}$$

Let us now normalize Equation (A4) by $\sqrt{N_n}$, where N_n can be calculated as follows:

$$N_n = \int_0^1 \psi_n^2(z)dz = \int_0^1 \sin^2(\beta_n z)dz = \frac{1}{2}. \tag{A5}$$

Hence, the normalized eigenfunctions are given by

$$\psi_n(z) = \frac{\Psi_n(z)}{\sqrt{N_n}} = \frac{\sin(\beta_n z)}{\sqrt{1/2}}. \tag{A6}$$

(*ii*) *Derivation of* $f(z)$ *in Equation* (49): The initial condition given in Equation (49) can be derived as follows. For $T = 0$, the forward transform (Equation 45) can be written as

$$\bar{S}_n(0) = \int_0^1 U(z, T = 0)\,\psi_n(z)\,dz. \tag{A7}$$

In terms of the z variable, for $T = 0$, Equation (31) gives

$$U(z, T = 0) = S(z, T = 0) - f(z). \tag{A8}$$

Enforcing the initial condition in Equation (28), Equations (A7) and (A8) reduces to

$$\bar{S}_n(0) = \int_0^1 [0 - f(z)]\psi_n(z)\,dz, \qquad n = 1, 2, 3, \ldots. \tag{A9}$$

Replacing the dummy index n by m, we obtain

$$\bar{S}_m(0) = \int_0^1 [0 - f(z)]\psi_m(z)\,dz, \qquad m = 1, 2, 3, \ldots. \tag{A10}$$

Equation (A10) requires the expression for $f(z)$, which can be obtained by solving Equations (32)–(34). Here, we employ the standard finite-difference method (FDM) to compute $f(y)$. Once $f(y)$ is determined, the corresponding $f(z)$ can be obtained using the transformation between y and z given in Equation (36). The detailed procedure for obtaining $f(y)$ is outlined below.

Using a uniform grid $y_j = a + (j-1)\Delta y$, $j = 1, \ldots, N_f$, with $\Delta y = (1 - a)/(N_f - 1)$, the derivatives at interior nodes $j = 2, \ldots, N_f - 1$ are approximated by central differences:

$$\left.\frac{d^2 f}{dy^2}\right|_{y_j} \approx \frac{f_{j+1} - 2f_j + f_{j-1}}{\Delta y^2}, \qquad \left.\frac{df}{dy}\right|_{y_j} \approx \frac{f_{j+1} - f_{j-1}}{2\Delta y}. \tag{A11}$$

Substituting these into the ODE (Equation 32) yields the discrete equation

$$K_j \frac{f_{j+1} - 2f_j + f_{j-1}}{\Delta y^2} + (K_j' + V_j)\frac{f_{j+1} - f_{j-1}}{2\Delta y} + V_j' f_j = 0, \tag{A12}$$

which can be written in tridiagonal form as

$$a_-^{(j)} f_{j-1} + a_0^{(j)} f_j + a_+^{(j)} f_{j+1} = 0, \tag{A13}$$

where

$$a_-^{(j)} = \frac{K_j}{\Delta y^2} - \frac{K_j' + V_j}{2\Delta y}, \quad a_0^{(j)} = -\frac{2K_j}{\Delta y^2} + V_j', \quad a_+^{(j)} = \frac{K_j}{\Delta y^2} + \frac{K_j' + V_j}{2\Delta y}. \tag{A14}$$

The boundary conditions (Equations 33 and 34) are enforced directly as

$$f_1 = S_a \quad \text{at} \quad y = a, \qquad f_{N_f} = 0 \quad \text{at} \quad y = 1, \tag{A15}$$

resulting in a tridiagonal linear system

$$A_f \mathbf{f} = \mathbf{b}, \qquad \mathbf{f} = [f_1, f_2, \ldots, f_N]^T. \tag{A16}$$

This system was solved in MATLAB using the sparse direct solver:

$$\mathbf{f} = A_f \backslash \mathbf{b}. \tag{A17}$$

(*ii*) *Construction of the system of ODEs* (*Equation* 50): Using the orthogonality condition defined in Equation (44), Equation (48) can be re-written as

$$\frac{d\bar{S}_m}{dT} = \sum_{n=1}^{\infty} \bar{S}_n(T)\left[-\beta_n^2 \int_0^1 \frac{K(z)}{(1-a)^2}\psi_n(z)\psi_m(z)dz + \int_0^1 \left\{\frac{1}{1-a}\frac{\partial K(z)}{\partial z} + V(z)\right\}\frac{1}{1-a}\frac{d\psi_n(z)}{dz}\psi_m(z)dz + \int_0^1 \frac{1}{1-a}\frac{\partial V(z)}{\partial z}\psi_n(z)\psi_m(z)dz\right], \quad \text{for} \quad m = 1, 2, 3, \ldots. \tag{A18}$$

The terms inside the square brackets of Equation (A18) are denoted by g_{mn}. Consequently, Equation (A18) can be rewritten as

$$\frac{d\bar{S}_m}{dT} = \sum_{n=1}^{\infty} \bar{S}_n(T) g_{mn}, \quad \text{for} \quad m = 1, 2, 3, \ldots. \tag{A19}$$

As we consider $n = N$ to denote the total number of terms retained in the truncated series, Equation (A19) can be expressed as

$$\frac{d\bar{S}_m}{dT} = \sum_{n=1}^{N} g_{mn}\,\bar{S}_n(T), \quad m = 1, 2, \ldots, N. \tag{A20}$$

This system of ODEs, together with the initial condition given by Equation (49), can be written compactly in matrix form as

$$\boldsymbol{A}\frac{d\boldsymbol{S}(T)}{dT} = \boldsymbol{G}\boldsymbol{S}(T), \quad \boldsymbol{S}(T = 0) = \boldsymbol{S}_0, \tag{A21}$$

where $\boldsymbol{A} = \boldsymbol{I}_{N\times N}$, the identity matrix of order $N \times N$. The expressions of $\boldsymbol{S}(T)$, $\boldsymbol{G}$, and $\boldsymbol{S}_0$ are as follows:

$$\boldsymbol{S}(T) = \begin{bmatrix} \bar{S}_1(T) \\ \bar{S}_2(T) \\ \vdots \\ \bar{S}_N(T) \end{bmatrix}, \quad \boldsymbol{G} = \begin{bmatrix} g_{11} & g_{12} & \cdots & g_{1N} \\ g_{21} & g_{22} & \cdots & g_{2N} \\ \vdots & \vdots & \ddots & \vdots \\ g_{N1} & g_{N2} & \cdots & g_{NN} \end{bmatrix}, \quad \text{and}$$

$$\boldsymbol{S}_0 = \begin{bmatrix} -\int_0^1 f(z)\psi_1(z)\,dz \\ -\int_0^1 f(z)\psi_2(z)\,dz \\ \vdots \\ -\int_0^1 f(z)\psi_N(z)\,dz \end{bmatrix}.$$

The coefficient matrix $\boldsymbol{G}$ was evaluated through numerical integration, and the initial vector $\boldsymbol{S}_0$ was also obtained numerically. The resulting system of first-order ODEs (Equation A21) was then solved using an explicit Runge–Kutta integration scheme, which efficiently captures the transient evolution of $\bar{S}_m$ while maintaining numerical stability. The values of N and N_f were set to 30 and 101, respectively. The Runge–Kutta integration was carried out over a time interval from $T = 0$ s to the prescribed end time, with adequately spaced time points. A relative tolerance of 1×10^{-4} and an absolute tolerance of 1×10^{-4} were used, ensuring sufficient temporal resolution for accurately capturing the transient evolution of the concentration profiles.

Appendix B: Detailed Finite Volume Discretization of the Governing Equations

The detailed FVM discretization corresponding to the governing equation is presented herein. Integrating Equation (27) over the control volume and across a time interval from T to $T + \Delta T$ yields

$$\int_T^{T+\Delta T}\left[\int_{\Omega_i}\frac{\partial S(y,T)}{\partial T}d\Omega\right]dT = \int_T^{T+\Delta T}\left[\int_{\Omega_i} K(y)\frac{\partial^2 S(y,T)}{\partial y^2}d\Omega\right]dT + \int_T^{T+\Delta T}\left[\int_{\Omega_i}\left\{\frac{\partial K(y)}{\partial y} + V(y)\right\}\frac{\partial S(y,T)}{\partial y}d\Omega\right]dT + \int_T^{T+\Delta T}\left[\int_{\Omega_i}\frac{\partial V(y)}{\partial y}S(y,T)d\Omega\right]dT. \tag{B1}$$

Utilizing first-order Euler backward (implicit) for time discretization and applying Gauss's divergence theorem where required, the aforementioned equation simplifies to

$$(S_i^{l+1} - S_i^l)\Delta\Omega_i = K(y)\left[\left(A\frac{\partial S}{\partial y}\right)_{i+1/2}^{l+1} - \left(A\frac{\partial S}{\partial y}\right)_{i-1/2}^{l+1}\right]\Delta T + \left\{\frac{\partial K(y)}{\partial y} + V(y)\right\}\left[(AS)_{i+1/2}^{l+1} - (AS)_{i-1/2}^{l+1}\right]\Delta T + \frac{\partial V(y)}{\partial y}S_i^{l+1}(\Delta\Omega_i)(\Delta T). \tag{B2}$$

Here, S_i^l and S_i^{l+1} represent the cell-averaged value of S over Ω_i at times T and $T + \Delta T$, respectively, denoted as

$$S_i^l = \frac{1}{\Omega_i}\int_{\Omega_i} S(y, T)d\Omega, \tag{B3}$$

and

$$S_i^{l+1} = \frac{1}{\Omega_i}\int_{\Omega_i} S(y, T + \Delta T)d\Omega, \tag{B4}$$

where $\Delta\Omega_i(= A\Delta y)$ denotes the volume of the target cell i, with A indicating the face area of said target cell. In order to derive the suitable form of the discretized equations from Equation (B2), the face center values $S_{i+1/2}^{l+1}$ and $S_{i-1/2}^{l+1}$, as well as the face center gradient values $\left(\frac{\partial S}{\partial y}\right)_{i+1/2}^{l+1}$ and $\left(\frac{\partial S}{\partial y}\right)_{i-1/2}^{l+1}$, are needed at the faces $i + 1/2$ and $i - 1/2$ respectively. Utilizing a second-order central difference scheme for the gradient face center values leads to the following expressions:

$$\left(\frac{\partial S}{\partial y}\right)_{i+1/2}^{l+1} = \frac{S_{i+1}^{l+1} - S_i^{l+1}}{\Delta y}, \tag{B5}$$

and

$$\left(\frac{\partial S}{\partial y}\right)_{i-1/2}^{l+1} = \frac{S_i^{l+1} - S_{i-1}^{l+1}}{\Delta y}. \tag{B6}$$

The face center values of S at the face centers $i + 1/2$ and $i - 1/2$, are determined using a quadratic upwind differencing scheme known as the QUICK (quadratic upstream interpolation for convective kinetics) scheme in the following manner [58]:

$$S_{i+1/2}^{l+1} = \frac{6}{8}S_i^{l+1} + \frac{3}{8}S_{i+1}^{l+1} - \frac{1}{8}S_{i-1}^{l+1}, \tag{B7}$$

and

$$S_{i-1/2}^{l+1} = \frac{6}{8}S_{i-1}^{l+1} + \frac{3}{8}S_i^{l+1} - \frac{1}{8}S_{i-2}^{l+1}. \tag{B8}$$

By substituting Equations (B5)–(B8) in Equation (B2), the discretized equation incorporating the QUICK scheme for the face center values and central differencing for the gradient terms can be expressed in a concise form as follows:

$$-\frac{1}{8}\mathrm{Y}_y S_{i-2}^{l+1} - \left(\mathrm{Y}_{yy} - \frac{7}{8}\mathrm{Y}_y\right)S_{i-1}^{l+1} + \left(1 + 2\mathrm{Y}_{yy} - \frac{3}{8}\mathrm{Y}_y - \mathrm{Y}\right)S_i^{l+1} - \left(\mathrm{Y}_{yy} + \frac{3}{8}\mathrm{Y}_y\right)S_{i+1}^{l+1} = S_i^l. \tag{B9}$$

The mathematical expressions for the coefficients, denoted as Y_{yy}, Y_y, and Y, are as follows:

$$\mathrm{Y}_{yy} = K(y)\frac{\Delta T}{(\Delta y)^2}, \tag{B10}$$

$$\mathrm{Y}_y = \left\{\frac{\partial K(y)}{\partial y} + V(y)\right\}\frac{\Delta T}{\Delta y}, \tag{B11}$$

and

$$\mathrm{Y} = \frac{\partial V(y)}{\partial y}\Delta T. \tag{B12}$$

The discretized equation (B9) is applicable to the internal nodes 3, 4, …, $n_{cell} - 1$. However, special attention is required for the nodes closest to the boundaries, such as 1, 2, and n_{cell}. In the QUICK scheme, the S-value at face centers is calculated using the formulas provided by Equations (B7) and (B8), which involve three nodal values. At the boundary node 1, S is given at the south face $i - 1/2$ as $S_{i-1/2} = S_{BS}$, but there is no south $(i - 1)$ node available to evaluate $S_{i+1/2}$ at the north face using Equation (B7). To address this issue, following the approach of Leonard [59], a linear extrapolation is performed to create a mirror node at a distance of $(\Delta y)/2$ to the south of the physical boundary. This extrapolation to the mirror node provides the required S node for the formula given by Equation (B7), which calculates $S_{i+1/2}$ at the north face of the target cell 1. Consequently, the expression for $S_{i+1/2}^{l+1}$ can be formulated as follows:

$$S_{i+1/2}^{l+1} = \frac{7}{8}S_i^{l+1} + \frac{3}{8}S_{i+1}^{l+1} - \frac{2}{8}S_{BS}^{l+1}. \tag{B13}$$

The face center value at the south face can be directly obtained from the provided boundary condition as follows:

$$S_{i-1/2}^{l+1} = S_{BS}^{l+1}. \tag{B14}$$

The gradient term at the face centers has been computed using the following expressions:

$$\left(\frac{\partial S}{\partial y}\right)_{i+1/2}^{l+1} = \frac{S_{i+1}^{l+1} - S_i^{l+1}}{\Delta y}, \tag{B15}$$

and

$$\left(\frac{\partial S}{\partial y}\right)_{i-1/2}^{l+1} = \frac{-8S_{BS}^{l+1} + 9S_i^{l+1} - S_{i+1}^{l+1}}{3\Delta y}. \tag{B16}$$

Using Equations (B13)–(B16) in Equation (B2), the discretized equation at node 1 results in:

$$\left(1 + 4\mathrm{Y}_{yy} - \frac{7}{8}\mathrm{Y}_y - \mathrm{Y}\right)S_i^{l+1} - \left(\frac{4}{3}\mathrm{Y}_{yy} + \frac{3}{8}\mathrm{Y}_y\right)S_{i+1}^{l+1} = S_i^l + \left(\frac{8}{3}\mathrm{Y}_{yy} - \frac{5}{4}\mathrm{Y}_y\right)S_{BS}^{l+1}. \tag{B17}$$

For cell 2, the following approximations can be made for the face center values and the gradient values:

$$\left(\frac{\partial S}{\partial y}\right)_{i+1/2}^{l+1} = \frac{S_{i+1}^{l+1} - S_i^{l+1}}{\Delta y}, \tag{B18}$$

$$\left(\frac{\partial S}{\partial y}\right)_{i-1/2}^{l+1} = \frac{S_i^{l+1} - S_{i-1}^{l+1}}{\Delta y}, \tag{B19}$$

$$S_{i+1/2}^{l+1} = \frac{6}{8}S_i^{l+1} + \frac{3}{8}S_{i+1}^{l+1} - \frac{1}{8}S_{i-1}^{l+1}, \tag{B20}$$

and

$$S_{i-1/2}^{l+1} = \frac{7}{8}S_{i-1}^{l+1} + \frac{3}{8}S_i^{l+1} - \frac{2}{8}S_{BS}^{l+1}. \tag{B21}$$

Utilizing Equations (B18)–(B21) within Equation (B2), the discretized equation for cell 2 takes the following form:

$$-\left(\mathrm{Y}_{yy}-\mathrm{Y}_{y}\right)S_{i-1}^{l+1}+\left(1+2\mathrm{Y}_{yy}-\frac{3}{8}\mathrm{Y}_{y}-\mathrm{Y}\right)S_{i}^{l+1}$$
$$-\left(\mathrm{Y}_{yy}+\frac{3}{8}\mathrm{Y}_{y}\right)S_{i+1}^{l+1}=S_{i}^{l}+\frac{2}{8}\mathrm{Y}_{y}S_{BS}^{l+1}. \tag{B22}$$

At cell n_{cell}, the face center values and the gradient values at the face centers can be approximated as follows:

$$\left(\frac{\partial S}{\partial y}\right)_{i+1/2}^{l+1}=\frac{8S_{BN}^{l+1}-9S_{i}^{l+1}+S_{i-1}^{l+1}}{3\Delta y}, \tag{B23}$$

$$\left(\frac{\partial S}{\partial y}\right)_{i-1/2}^{l+1}=\frac{S_{i}^{l+1}-S_{i-1}^{l+1}}{\Delta y}, \tag{B24}$$

$$S_{i+1/2}^{l+1}=S_{BN}^{l+1}, \tag{B25}$$

and

$$S_{i-1/2}^{l+1}=\frac{6}{8}S_{i-1}^{l+1}+\frac{3}{8}S_{i}^{l+1}-\frac{1}{8}S_{i-2}^{l+1}, \tag{B26}$$

where S_{BN}^{l+1} is the S value at the face center $i+1/2$ of the target cell n_{cell}. Using (B23)–(B26) in Equation (B2), the discretized equation at cell n_{cell} is written as follows:

$$-\frac{1}{8}\mathrm{Y}_{y}S_{i-2}^{l+1}-\left(\frac{4}{3}\mathrm{Y}_{yy}-\frac{6}{8}\mathrm{Y}_{y}\right)S_{i-1}^{l+1}+\left(1+4\mathrm{Y}_{yy}+\frac{3}{8}\mathrm{Y}_{y}-\mathrm{Y}\right)S_{i}^{l+1}$$
$$=S_{i}^{l}+\left(\frac{8}{3}\mathrm{Y}_{yy}+\mathrm{Y}_{y}\right)S_{BN}^{l+1}. \tag{B27}$$

In a concise format, the discretized equations for all the cells (Equations B9, B17, B22 and B27) can be expressed as follows:

$$a_{i-2}S_{i-2}^{l+1}+a_{i-1}S_{i-1}^{l+1}+a_{i}S_{i}^{l+1}+a_{i+1}S_{i+1}^{l+1}=r_{i}, \tag{B28}$$

where a_{i-2}, a_{i-1}, a_i, and a_{i+1} represent the corresponding coefficients of the cell values S_{i-2}^{l+1}, S_{i-1}^{l+1}, S_{i}^{l+1}, and S_{i+1}^{l+1}, respectively. For instance, for Equation (B27), the expressions for the coefficients a_{i-2}, a_{i-1}, a_i, and a_{i+1} are as follows:

$$a_{i-2}=-\frac{1}{8}\mathrm{Y}_{y}, \tag{B29}$$

$$a_{i-1}=-\left(\frac{4}{3}\mathrm{Y}_{yy}-\frac{6}{8}\mathrm{Y}_{y}\right), \tag{B30}$$

$$a_{i}=\left(1+4\mathrm{Y}_{yy}+\frac{3}{8}\mathrm{Y}_{y}-\mathrm{Y}\right), \tag{B31}$$

$$a_{i+1}=0, \tag{B32}$$

and

$$r_{i}=S_{i}^{l}+\left(\frac{8}{3}\mathrm{Y}_{yy}+\mathrm{Y}_{y}\right)S_{BN}^{l+1}. \tag{B33}$$

Equation (B28) will form a system of n_{cell} number of linear equations with n_{cell} number of unknowns. This system of linear equations is solved using the Gauss–Seidel iteration technique. The Gauss–Seidel iteration commences with the initial guess value of $[S_1^{l+1}|^{(0)}\cdots S_{n_{cell}}^{l+1}|^{(0)}]$. The Gauss–Seidel step is written as:

$$S_{i}^{l+1}|^{(p)}=S_{i}^{l+1}|^{(p-1)}$$
$$+\frac{1}{a_{i}}\left[r_{i}-\left(a_{i-2}S_{i-2}^{l+1}|^{(p)}+a_{i-1}S_{i-1}^{l+1}|^{(p)}+a_{i}S_{i}^{l+1}|^{(p-1)}+a_{i+1}S_{i+1}^{l+1}|^{(p-1)}\right)\right]. \tag{B34}$$

In a condensed form, the above equation becomes:

$$S_{i}^{l+1}|^{(p)}=S_{i}^{l+1}|^{(p-1)}+\frac{Res_{i}}{a_{i}}, \tag{B35}$$

where

$$Res_{i}=r_{i}-\left(a_{i-2}S_{i-2}^{l+1}|^{(p)}+a_{i-1}S_{i-1}^{l+1}|^{(p)}+a_{i}S_{i}^{l+1}|^{(p-1)}+a_{i+1}S_{i+1}^{l+1}|^{(p-1)}\right). \tag{B36}$$

This is valid for all cells i and iteration steps, $p \geq 1$. To track convergence, the residual error in a specific iteration p for a given cell i is calculated as follows:

$$\epsilon_{i}^{(p)}=S_{i}^{l+1}|^{(p)}-S_{i}^{l+1}|^{(p-1)}. \tag{B37}$$

Moreover, convergence is defined as the state when the following criterion is satisfied: the root mean square is less than or equal to a certain tolerance level $eps_{\max}$, denoted as

$$\sqrt{\frac{1}{n_{cell}}\sum_{\forall i}\left(\epsilon_{i}^{(p)}\right)^{2}}\leq\epsilon_{max}. \tag{B38}$$

In the current study, $\epsilon_{\max}$ has been set to 10^{-6}. For the numerical simulations, a total of 100 cells ($n_{cell}=100$) of uniform size in the vertical direction have been used, with a time step size of $\Delta T=0.001$ s.

Appendix C: Convergence Evaluation of *ga–fmincon* Calibration

The convergence behavior of the hybrid optimization scheme was assessed using the following plots, based on a single randomly selected run (RUN SC).

The convergence curve (Figure C1) presents the objective function values (Equation 52) over iterations. The objective function decreases sharply during the initial iterations, followed by minor fluctuations before reaching an approximately constant value. These fluctuations are small and do not affect the final optimized parameters, indicating stable and monotonic convergence. Collectively, the plots support the effectiveness and stability of the hybrid *ga–fmincon* approach for calibrating Λ and σ in this study.

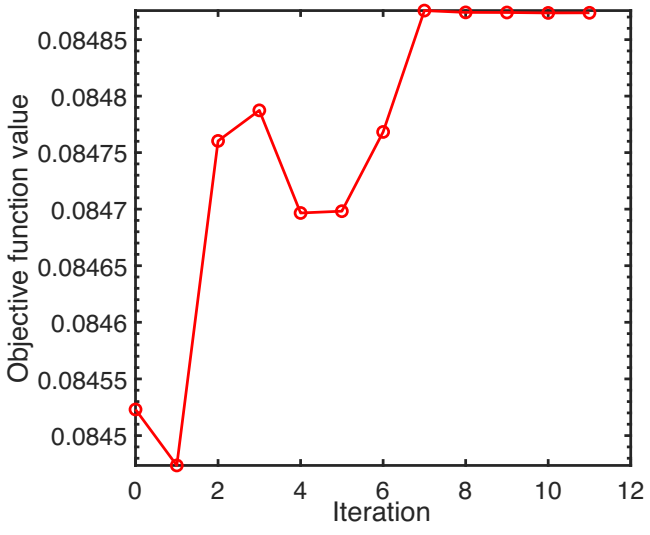

FIGURE C1 | Convergence plots of the optimization scheme for RUN-SC.